

© 2018 Caitlin M. Race

PHOTONIC CRYSTAL ENHANCED LIGHT EMITTERS AND THEIR USE
IN IMPROVING CANCER SCREENING AND DISEASE PROGRESSION
MONITORING

BY

CAITLIN M. RACE

DISSERTATION

Submitted in partial fulfillment of the requirements
for the degree of Doctor of Philosophy in Electrical and Computer Engineering
in the Graduate College of the
University of Illinois at Urbana-Champaign, 2018

Urbana, Illinois

Doctoral Committee:

Professor Brian Cunningham, Chair
Professor Gary Eden
Associate Professor Viktor Gruev
Assistant Professor Andrew Smith

ABSTRACT

Screening for and monitoring the progression of cancer remains a complex task in medicine today, further complicated by the variety of both cancer types and treatments. Each patient's response to treatments and cancers is unique, calling for a personalized approach to healthcare. Early detection and correct treatment of cancer are critical for controlling disease progression and improving patient outcomes.

This dissertation describes a photonic crystal-based detection and analysis system to improve cancer screening and treatment by increasing sensitivity to low concentrations of cancer biomarkers. There are two main methods of increasing sensitivity: automating detection and analysis to reduce time and user error, and improving coupling efficiency by optimizing photonic crystal design parameters. I address both these methods in this work: the former by increasing sensitivity in the screening for oropharyngeal cancer, and the latter in the design of two new photonic crystals. The first of these photonic crystals is designed for enhanced excitation of multi-colored quantum dots, instead of traditional fluorescent dyes, for the investigation of multiplexed treatment progression monitoring of prostate cancer. The second of these photonic crystals is a design for metamaterial-based photonic crystals that improves coupling efficiency and offers additional design flexibility. This new photonic crystal is interchangeable with the photonic crystal designed to enhance quantum dots but can also be used in a standard microscope setup. The objective is to retain high enhancement while improving coupling to the photonic crystal resonance to increase fluorescent output.

This work presents my efforts toward the development of technologies that will enable low-cost, portable screening and disease monitoring to improve outcomes for patients around the world. The ultimate goal is to improve patient access to vital healthcare practices while keeping expenses low and standard of detection high.

To my teachers

ACKNOWLEDGMENTS

First and foremost, I would like to express my gratitude to my adviser, Professor Brian Cunningham. His methods of support and encouragement during this time were a driving factor in my success. I have learned invaluable lessons under his guidance that I will carry with me throughout my professional career.

Next, I would like to thank my committee members: Professor Gary Eden, Professor Viktor Gruev, and Professor Andrew Smith. Their feedback and encouragement during this process were greatly appreciated. I would also be remiss not to acknowledge the MNTL business office and cleanroom staff. My fellow grad students and I would not get anything done if it were not for all of their hard work.

Spending time with and learning from members of the NSG group and other people at the U of I have truly been the best part of this experience. I would especially like to acknowledge: Dr. Yue Zhuo, my desk mate and the first person to make me feel truly welcome in the lab; Phuong Le, whose frequent visits to my desk to steal chocolate and leave post-it notes were the highlight of my day; Dr. Gloria See, whose perspective and advice resonated with me during some of my most difficult times; the various groups on campus and around Champaign-Urbana who have welcomed me with open arms; and my friends around the country who have kept reminding me that there is life beyond graduate school.

I need to thank my family as well: my parents, who responded to my decision to go to grad school (again) with “What took you so long?!”; my sister, who, despite living 500+ miles away, was my closest confidant and kept me grounded in reality; and my aunt and uncle, for their home-away-from-home and constant positive thoughts. They all have always believed in me and sometimes seemed to know me better than I know myself.

Finally, I could not have done any of this without the unconditional support of my fiancée, Brad, and our dogs, Carmel and Shadow. They were with me day in and day out: commiserating all the lows, celebrating all the highs, and dragging me outside for daily walks and lots and lots of ice cream.

TABLE OF CONTENTS

	Page
LIST OF ABBREVIATIONS	vi
LIST OF SYMBOLS	viii
CHAPTER 1 INTRODUCTION	1
1.1 Motivation	1
1.2 Background	3
1.3 Competing Approaches	5
1.4 Dissertation Structure	12
CHAPTER 2 PHOTONIC CRYSTAL ENHANCED FLUORESCENCE DETECTION AND ANALYSIS OF AN ANTIVIRAL ANTIBODY CANCER BIOMARKER IN SERUM	13
2.1 Introduction	13
2.2 Methods	16
2.3 Results and Discussion	20
2.4 Conclusion	23
CHAPTER 3 A NEW SYSTEM FOR EXCITATION AND DETEC- TION OF QUANTUM DOTS USING PHOTONIC CRYSTALS	24
3.1 Introduction	24
3.2 Device Structure	25
3.3 Results and Discussion	31
3.4 Conclusion and Future Work	37
CHAPTER 4 THE APPLICATION OF HYPERBOLIC METAMA- TERIALS TO ENHANCE QUANTUM DOT-BASED BIOSENSORS	38
4.1 Introduction	38
4.2 Device Structure	40
4.3 Results and Discussion	45
4.4 Conclusion and Future Work	50
CHAPTER 5 PHOTONIC CRYSTAL ENHANCED QUANTUM DOT EMISSION FOR MONITORING TREATMENT EFFICACY IN METASTATIC CASTRATE-RESISTANT PROSTATE CANCER	52
5.1 Introduction	52
5.2 Methods	57
5.3 Conclusion and Future Work	59
CHAPTER 6 CONCLUSIONS	61
REFERENCES	62

LIST OF ABBREVIATIONS

AR-FL	Full-Length Androgen Receptor
AR-V	Androgen Receptor Variant
dPCR	Digital PCR
EMA	Effective Medium Approximation
FDTD	Finite Difference Time Domain
FISH	Fluorescence <i>In Situ</i> Hybridization
FWHM	Full Width Half Maximum
GMRF	Guided-Mode Resonant Filter
HMM	Hyperbolic Metamaterial
HPV	Human Papillomavirus
LSPR	Localized Surface Plasmon Resonance
mRNA	Messenger RNA
mCRPC	Metastatic Castrate-Resistant Prostate Cancer
NA	Numerical Aperture
OPC	Oropharyngeal Cancer
PC	Photonic Crystal
PCEF	Photonic Crystal Enhanced Fluorescence
PHC	Photonic Hypercrystal
PSA	Prostate-Specific Antigen
QD	Quantum Dot
qRT-PCR	Real-Time Qualitative PCR
RCWA	Rigorous Coupled Wave Analysis
RI	Refractive Index

RIU	Refractive Index Unit
ssDNA	Single-Stranded DNA
SERS	Surface-Enhanced Raman Scattering
SPR	Surface Plasmon Resonance
TIR	Total Internal Reflection
TE	Transverse Electric
TM	Transverse Magnetic
WGM	Whispering Gallery Mode

LIST OF SYMBOLS

β, k	Propagation constant
c	Speed of light
d	Spectrometer grating spacing
ε	Permittivity
f	Focal length
f_c	Duty cycle
ff	Fill factor
h	Grating depth
ℓ	Grating lines
Λ	Grating period (1D)/lattice constant (2D)
λ	Wavelength
m	Waveguide mode
M	Magnification
μ	Permeability
n	Refractive index
p	Vertical period height
ϕ	Angle of incidence
Q	Quality factor
r	Radius
t_l	Thickness of layer l
w	Width
ω	Radial frequency

CHAPTER 1

INTRODUCTION

1.1 Motivation

Cancer screening is a critical part of medical practice today. It is generally agreed that early diagnosis of cancer leads to better outcomes including reduction of side effects and improved life expectancy, as shown in Fig. 1.1 [1, 2]. Cancer is also more easily treated before the disease has metastasized and a patient starts to show symptoms. Screening is especially important for certain types of cancers, including breast, cervix, mouth, larynx, colon, rectum, and skin [3]. However, reliable screening depends on an understanding of the disease being screened for and an accepted treatment plan [4]. Cancer itself is still not fully understood - with multiple disease pathways and individual genetic mutations, it is difficult to accurately diagnose the cause of every cancer and prescribe the correct treatment [3]. Once treatment has begun, it is also important to monitor the disease progression to determine if the prescribed drug therapy regimen is effective.

According to the 2014 World Cancer Report, there were 14.1 million new cancer diagnoses worldwide and 8.2 million estimated cancer deaths in 2012 [3]. Cancer incidence increases with age as cells break down and acquire more mutations. Regions of the world differ in which cancers are most common, but the disease is a global problem without a universal cure. Some cancers, like lung cancer, are frequently preventable, but others, like childhood cancer, are unpredictable and often fatal without the correct intervention early in the disease lifetime [3]. With the ubiquity of the disease, it is likely that even if someone has not had cancer, she would know somebody affected.

Biosensors are a crucial part in the fight against cancer. These devices convert changes in biology to detectable signals (light, in this case) [6]. My research focuses on *in vitro* sensing using blood samples. These blood samples contain biomarkers, which are targets of interest for disease and include cells,

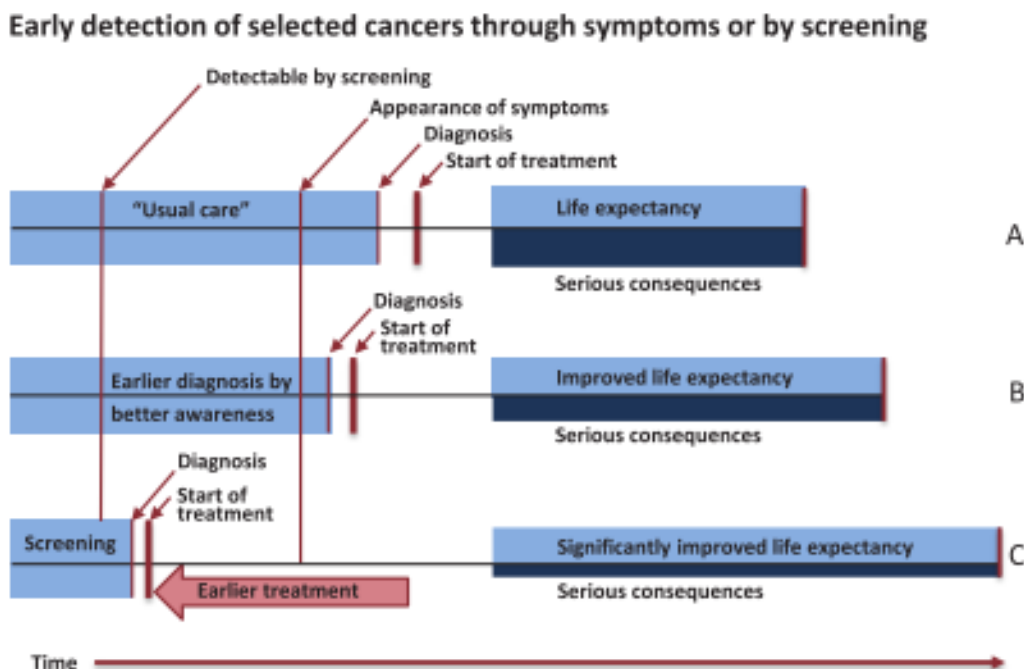


Fig. 1.1. Life expectancy and treatment timelines after cancer detection for various scenarios: (A) “usual care,” (B) early detection, and (C) detection as early as possible. Reproduced from Ref. [3], which was adapted from Ref. [5].

bacteria, viruses, proteins, hormones, enzymes, and nucleic acids [6]. Different biomarkers are specific to screening or monitoring treatment of different cancers, but they can typically be detected with a tag, such as a fluorophore [7], a gold nanoparticle [8], a Raman dye [9], or simply detected by themselves in a “label-free” environment [10]. Regardless of the detection method, there is a critical need for biosensors with high specificity and sensitivity to accurately screen or track cancer, especially in its early stages when cancer cells and biomarkers exist in ultra-low concentrations [11].

Thus, cancer screening, diagnosis, and treatment depend on advancements not only in cancer biology, but also in sensing methods to indicate the presence or absence of biomarkers for cancer screening and treatment progression. My research focuses on two types of cancer: oropharyngeal cancer (OPC) and metastatic castrate-resistant prostate cancer (mCRPC). The ultimate goal is to have a universal platform for disease monitoring and screening that can be easily applied to indicators of different cancers and to treatment progressions. In this work, I propose a photonic crystal (PC)-based solution for monitoring the biomarkers for these cancers. Before expanding on my research, I will present

an overview of PCs followed by exploring the advantages and disadvantages of competing light-based biosensors.

1.2 Background

Before discussing the Cunningham group’s current generation of PCs, I will give an overview of their predecessor, guided mode resonant filters (GMRFs). Researchers proved that by either fabricating a grating of one dielectric material on top of a separate dielectric material [12–14] or overcoating a dielectric grating with another dielectric material [15], a resonance anomaly could be achieved. These 1D, periodic structures were found to have resonance effects due to the formation of a guided wave inside the layers. In this case, the low-efficiency grating ($h/\lambda \ll 1$) couples light into the waveguide created by the alternating refractive indices (RIs) of the dielectric layers [15]. Norton describes these structures as having anomalies, where there is an overlap of the “sharp” (resonance) and “broad” (Rayleigh) anomalies. The resonant grating structures must contain a coupling mechanism (the grating), which excites “leaky” modes in the waveguide [16]. For most purposes, it is sufficient to account for only the zeroth (and possibly first) order modes.

In order for a resonance condition to occur, light inside the waveguide cavity should undergo constructive interference. This is described by the Bragg condition for a cavity depth d , average refractive index n , and an incident angle ϕ :

$$2nd \sin \phi = m\lambda$$

where the phase accumulated during a round trip path across the cavity is equal to an integer multiple m of the wavelength λ . Incident light not satisfying this condition will destructively interfere and a standing wave can form.

In addition to the Bragg condition, there is also a momentum matching condition to account for the effect of the grating periodicity on the wavelength of incoming light. This is described by

$$\beta_{mode} = \hat{x}|\beta_0| \sin(\phi_i) \pm \frac{2\pi}{\Lambda}$$

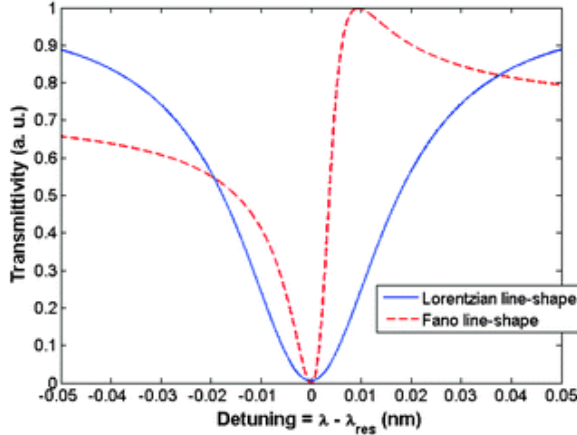


Fig. 1.2. Comparison of asymmetrical Fano (red) and symmetrical Lorentzian (blue) lineshapes. Reproduced from Ref. [18] with permission from The Royal Society of Chemistry.

where Λ is the grating period, β_0 and ϕ_i correspond to the incident light, and β_{mode} corresponds to the mode of the standing wave in the cavity ($|\beta| = \omega \sqrt{\mu\epsilon}$) [17].

Note that there are two resonance conditions: the first being a Fabry-Perot cavity with the Bragg condition and the second being a grating with momentum matching [17]. The combination of these two resonances (grating and Fabry-Perot) forms a Fano resonance [18] with the characteristic asymmetric lineshape [19] as shown in Fig. 1.2. Proper design of the grating and the Fabry-Perot cavity leads to a high-Q resonator, with the parameters of this resonance tunable by the design parameters of the grating-coupled cavity.

A PC consists of a periodic variation of dielectric materials in either 1, 2, or all 3 dimensions [20] with alternating high and low RI materials [21] (Fig. 1.3). PCs were first named as such by Yablonovitch and Gmitter in 1989 when they fabricated a 3D, face-centered-cubic array of Al_2O_3 spheres in dielectric foam, experimentally demonstrating a “photonic band gap,” the electromagnetic analog of an electronic band gap [22]. The simplest fabricated PC structure is a type of GMRF, or 1D square grating. Such a structure is typically expanded into 2D or 3D by etching holes or growing rods in a square, hexagonal, or even more complex array. Confinement of light in a PC, the photonic band gap, is due to a periodic RI variation, analogous to confinement of electrons, the electronic band gap, which is due to the periodic atomic structure in a crystal lattice [20]. Photonic band gap engineering is achieved by variations in material RIs, thickness of materials, the periodicity, and even defects. Typically, 1D PCs can confine light in only one direction, so 3D band gaps can only be achieved with 3D PCs [20].

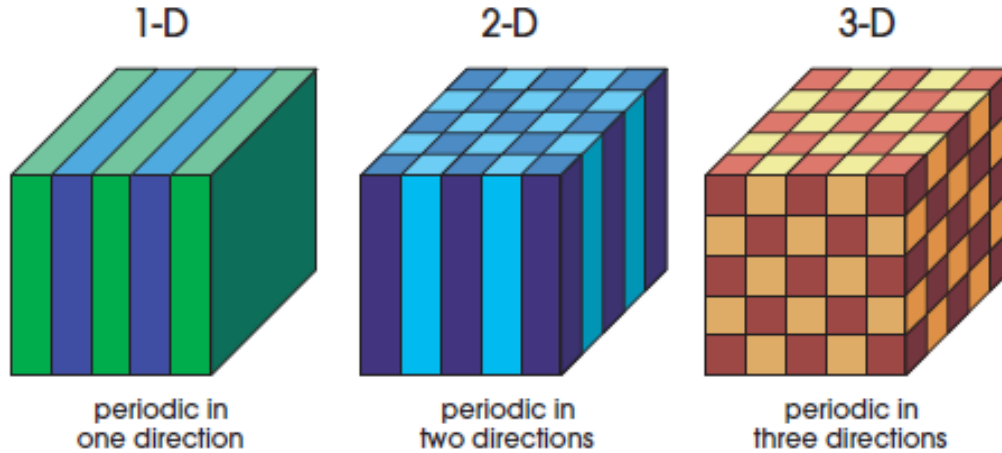


Fig. 1.3. Simple diagram of 1D, 2D, and 3D PCs in a square lattice. Different colors depict materials with varying dielectric constants. Reproduced from Ref. [20] with permission from Princeton University Press.

More information about PC fabrication and its use in my research can be found in the following chapters of this work.

1.3 Competing Approaches

While there are numerous types of biosensors, including electrochemical, acoustic, and impedance, I will limit the analysis here to light-based biosensors. These include ring resonators, waveguides/fibers, plasmonics, and Raman, as well as newly discovered optical phenomena [23–25]. Optical biosensors have the property of interacting with biological tags, such as fluorophores, that are common detection mechanisms. They are also highly compatible with traditional cleanroom fabrication techniques, meaning such devices can be easy to design, fast, low-cost, and integrated in lab-on-a-chip technologies [26]. Like the Cunningham group PCs, most of these approaches rely on the biomarkers being within the evanescent field region, typically extending ~ 100 nm from the surface [27]. RI differences of the biomolecules change the coupling conditions, and achieving the correct coupling conditions excites an evanescent field, which in turn can excite a fluorophore or other photon emitter on the surface (if not using label-free detection).

1.3.1 Waveguides

Like all optical biosensors, waveguides are sensitive to RI changes on the surface, making them good candidates for label-free detection [28]. There are two main types of waveguides: cylindrical and planar [29]. Optical fibers are a subset of cylindrical waveguides and are especially useful for remote sensing and applications requiring flexible devices. There are more complicated configurations of waveguides for confinement of light in two dimensions, including slot waveguides [30], rib waveguides [31], segmented waveguides [32], and strip waveguides [33]. These types of waveguides add variation in a second dimension in order to further control wave propagation.

In all cases, a high RI core is surrounded by a low RI cladding. Total internal reflection (TIR) occurs for an incident angle ϕ greater than the critical angle ϕ_c :

$$\phi_c = \sin^{-1} \left(\frac{n_2}{n_1} \right)$$

where n_1 is the RI of the core and n_2 is the RI of the cladding [34]. During TIR, an external evanescent field extends outside the cladding into the surrounding medium.

Despite their relative ease of fabrication, waveguides are not suitable for large-area, general-purpose biosensors. Depending on their configuration, there can be minimal extension of the evanescent field into surrounding medium, reducing sensitivity. Waveguides also frequently require a prism coupler or focusing optics in order to excite the resonant mode, increasing the device size and complexity [29].

A unique type of waveguide, called a zero-mode waveguide, is highly applicable for studying single-molecule processes at high concentrations [35]. These waveguides, fabricated by etching small ($r = 50$ nm) holes in metal (Al), enable the observation of real-time molecular activity, such as ligand binding events. Metal-clad waveguides, in contrast to typical dielectric waveguides, have a cutoff frequency below which no waves (or zero modes) will propagate [35]. At these frequencies, the “zero-mode waveguide” will contain an evanescent field inside the holes, exciting fluorescently labeled molecules.

1.3.2 Ring Resonators

Ring resonators, also called whispering gallery mode (WGM) resonators, were introduced as ultra-high sensitivity biosensors by Vollmer *et al.* in 2002 [36]. They have become especially popular for label-free, single nanoparticle detection [37, 38]. Their operation is analogous to acoustic whispering galleries, such as in St. Paul’s Cathedral in London [11]. In both cases, the wave travels around the gallery in such a way that it constructively interferes with itself at set intervals, based on TIR (Fig. 1.4). For optical biosensors, the resonant wavelength (λ_{res}) is defined as

$$\lambda_{\text{res}} = \frac{2\pi R n_{\text{eff}}}{m}$$

where R is the radius of the ring, n_{eff} is the effective RI, and m is a positive integer [18]. This is derived using the Bragg condition, except instead of traveling round trip through a cavity, the wave travels in a complete circle. Architectures for ring resonators include planar resonators, microspheres, microtoroids, and liquid core optical ring resonators.

RI sensing in WGM resonators is based on detection of the shift in n_{eff} in the medium surrounding the ring [18]. These RI changes lead to a shift in λ_{res} , which is frequently detected using simple white light absorption measurements.

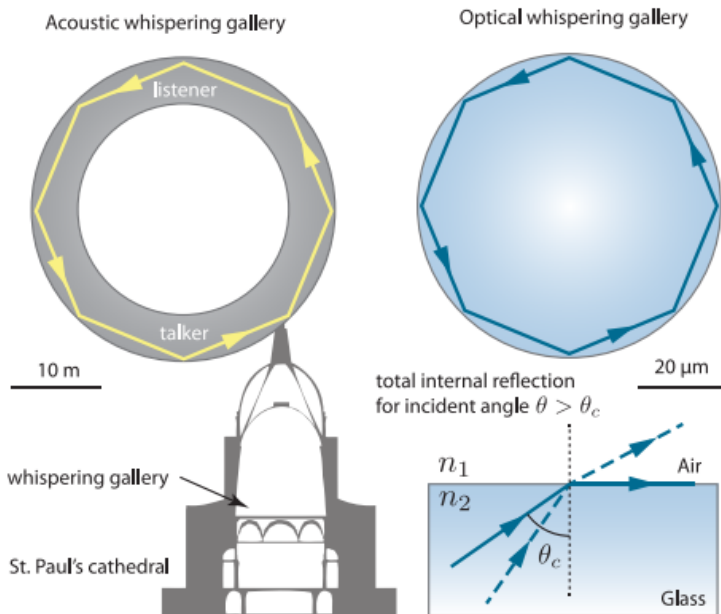


Fig. 1.4. Acoustic wave (left) and electromagnetic wave (right) depiction of a whispering gallery mode resonator. ©2015 Optical Society of America [11].

Like most label-free optical biosensors, a figure of merit is the resonance shift per change in RI, with units nm/Refractive Index Unit (RIU).

The resonance of WGM sensors can also be used to enhance other optical processes, including fluorescence and optical absorption, instead of detecting change in RI [18]. In both cases, the evanescent field from the ring interacts with the medium outside of the ring. This field can be used either to excite the fluorophores for fluorescence measurements or as a probe for absorption methods to estimate concentration [18].

While ring resonators are ideally suited for single-molecule detection, their device complexity is not very suitable for large-area, general-purpose biosensors. Large-scale fabrication of micro- and nano-sized rings becomes expensive, and the ring resonators start to interfere with each other if placed too closely together [18]. With nanoscale sensors, it also becomes difficult to guarantee co-location of the rings and molecules of interest without complicated preparation procedures.

1.3.3 Plasmonics

Unlike resonance effects in dielectrics caused by a change in RI, plasmon resonance is caused by electron oscillation in metals [39, 40]. This effect can result from either of two physical manifestations: surface plasmon resonance (SPR) and localized surface plasmon resonance (LSPR) [41]. SPR is the oscillation of electrons in a metal layer, while LSPR is oscillation of electrons in metal nanoparticles (Fig. 1.5a-b) [40]. Both of these phenomena have their advantages in biosensing.

The first use of SPR for label-free biosensing was by Englebienne in 1998 for real-time monitoring of antigen-antibody binding on a colloidal gold surface [42]. Like in waveguides and ring resonators, the resonance shift is due to a change in RI near the surface of the biosensor. In the case of the SPR sensor, a larger resonance shift implies that a larger mass has bound to the metal surface, making it more difficult for electrons to oscillate, resulting in a lower energy (red-shifted) resonance [42].

From SPR, researchers quickly moved to LSPR, as nanoparticles can much more easily be tuned to a desired resonance by altering their size and shape [40, 43, 44]. The metal layer used for SPR also suffers from several disadvantages:

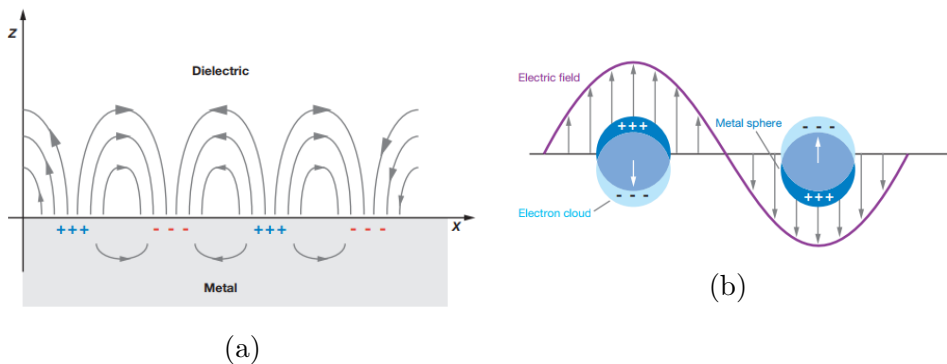


Fig. 1.5. Depictions of (a) a surface plasmon polariton (or propagating plasmon) and (b) a localized surface plasmon. Reproduced from Ref. [40] with permission from Annual Reviews.

first, the evanescent field travels too far into the neighboring dielectric layer, sending energy farther than needed to detect biomolecules; second, coupling into an SPR is difficult to achieve and usually requires a prism-coupler, increasing size and complexity of the device; finally, SPR surface waves propagate in the $10\ \mu\text{m}$ to $100\ \mu\text{m}$ range, meaning sensing applications smaller than that are not easily feasible [44].

The first LSPR device for biosensing was made by Haes and Van Duyne in 2005 for detection of a biomarker for Alzheimer’s disease [45]. Many biosensors have been fabricated since, using advances in nanotechnology to expand the scope of LSPR to plasmon-photon interactions [46], plasmonic nanorods [43], single-nanoparticle sensing [39], and plasmonic nanoantennas [47]. The enhancement of LSPR biosensors is naturally limited to the area around the nanoparticles, but the advantages of easier coupling and customization outweigh the smaller electric field magnitudes [44]. However, LSPR devices still present complications for biosensors, most notably the fact that metals are lossy. This lost energy is converted to heat radiating from the nanoparticles, which has the potential to compromise biological specimens [48–50].

1.3.4 Surface-Enhanced Raman Scattering

Surface-enhanced Raman scattering (SERS), like SPR and LSPR, depends on plasmon oscillations in metals for resonant field effects [40]. Instead of detecting RI changes or fluorescence, SERS enhances the detection of Raman spectra of

biomarkers or their Raman dye tags. The Raman effect was first published in 1928 by C.V. Raman. He noticed that, under bright illumination, the spectra of some liquids contained wavelengths not present in the illumination source [51]. These spectral lines were vibrational modes of the measured liquids, with different liquids having different Raman spectra. Instead of Rayleigh scattering, where an excited molecule relaxes back to its original state, Raman scattered molecules absorb some of the excitation energy into vibrational modes. Thus, for Stokes Raman scattering, the scattered wavelength will be longer (lower energy) than the excitation wave. While rarer, anti-Stokes Raman scattering occurs when an molecule in an excited vibrational state relaxes back down to the ground state. The amplitude of Raman spectral peaks is typically very small (representing about 10^{-6} of incident photons) and needs enhancement [52]. SERS, then, uses LSPR to enhance Raman spectra of molecules in the near-field of the nanoparticles used to generate the LSPR.

Raman scattering, and SERS in general, were initially used for structural and chemical analysis of molecules [52]. The first use of SERS for biosensing was in 1977 by Jeanmaire and Van Duyne for studying molecules adsorbed on the surface of silver electrodes [53]. Since that time, researchers have combined SERS with lateral flow assays [54, 55], waveguides [56], and nanohole arrays [57] to detect DNA, antibody-antigen binding events, and metal ions, as an example. All of these methods seek to either integrate SERS into more traditional biological sensing or to mitigate some of its disadvantages. Notably, like LSPR, the peak enhancement of SERS only occurs in close proximity to the nanoparticle, and metal nanoparticles are still subject to heating effects, potentially compromising the biological specimens.

1.3.5 Dielectric Nanoantennas

Dielectric nanoantennas arose from the need to overcome the heat radiated from typical metallic nanoparticles used for SERS and LSPR biosensing. Metallic nanoparticles are lossy, and the loss radiates as heat [48–50]. It is always desirable to minimize loss, but heat poses an additional problem for integration with biological specimens: the potential to damage the material under investigation. In the past few years, many research groups have successfully fabricated dielectric nanoantennas as simple arrays [58, 59] and dimers [48–50],

in contrast to the much wider array of shapes seen with metal nanoparticles (bowties, flowers, rods, etc).

These research efforts into dielectric nanoantennas have very recently inspired some research into nanoantenna biosensors. Both Yavas *et al.* and Bontempi *et al.* have fabricated silicon nanodisk arrays to detect prostate-specific antigen and biotin-streptavidin binding, respectively [58, 59]. They both show high sensitivity and real-time detection, hopefully driving the effort to more fully realize this new technology.

1.3.6 New Materials

In recent decades, new classes of biosensors have been reported that were previously undiscovered or simply not fabricatable with the latest technology. These materials, called metamaterials, were first fabricated in 1999, when Pendry *et al.* created a magnetic structure from nonmagnetic conducting sheets [60]. Metamaterials are engineered structures made of metal and/or dielectric materials that have properties not traditionally found in nature [61]. Such materials were theoretically predicted in Veselago's landmark 1968 paper discussing negative permittivities and permeabilities and their potential applications [62]. In theory, metamaterials can be used to fabricate perfect lenses [63], cloaking devices [64], flat lenses [65], and photonic hypercrystals [66], as well as used to generate a whole new class of surface waves called Dyakonov waves [67], among numerous other phenomena, many likely yet to be discovered. In reality, metamaterial performance is often limited by material losses and bandwidth limits, but advances in research and nanotechnology are closing these gaps.

There have been several recent publications of researchers using metamaterials and new physical phenomena to do biosensing. Most recent work is in the early stages: one paper demonstrates that Dyakonov waves can be used for biosensing [68]; others report the detection of single nanoparticles [69], single particles [70], or ultra-low concentrations of standard biomolecules [71]; and yet another demonstrates the capability of metamaterials to sense RI changes using simulations [72]. I expect that future research into metamaterial biosensors will make them more widely applicable and easier to fabricate.

1.4 Dissertation Structure

This dissertation is structured as follows:

- Chapter 2 describes a new software and analysis methodology for scanning and analyzing PCs using fluorophore-based detection. This system was used to image and analyze patient sample data for oropharyngeal cancer, paving the way for an all-in-one, low-cost, high sensitivity, disease screening system.
- Chapter 3 discusses a new PC and optical setup for enhancing excitation of quantum-dot tagged biomarkers instead of fluorophores. Unlike fluorophores, different quantum dots are excited at the same wavelength, so excitation of QDs with varying emission wavelengths can be used to effectively multiplex biomarker detection.
- Chapter 4 introduces a PC utilizing hyperbolic metamaterials that is compatible with the system developed in Chapter 3. This new device expands coupling conditions to make PCs more compatible with standard microscopes and other more portable optical setups.
- Chapter 5 includes a proposal for continuing the work of Chapter 3 by using quantum dot-tagged messenger RNA as an marker of treatment efficacy in metastatic castrate-resistant prostate cancer.

CHAPTER 2

PHOTONIC CRYSTAL ENHANCED FLUORESCENCE DETECTION AND ANALYSIS OF AN ANTIVIRAL ANTIBODY CANCER BIOMARKER IN SERUM

2.1 Introduction

We demonstrate the PCEF platform for detecting anti-E7 antibody, a biomarker for human papillomavirus (HPV)-associated oropharyngeal cancer (OPC), representing an application with a significant unmet clinical need that can benefit from point-of-care analysis. HPV is commonly associated with various cancers, and of the ~ 200 different types of HPV, 15 are considered high-risk [73]. Proteins produced early in the viral life cycle—specifically E6 and E7—are known to play important roles in initiating and maintaining the malignant transformation of host cells [73]. Forty to eighty percent of OPC cases have been attributed to HPV, and of these, up to 90% are caused by HPV16 [74]. Importantly, 46 – 50% and 63 – 69% of OPC cases have been demonstrated to be seropositive for HPV16 E6 and E7, respectively, with antibodies (IgG) to either E6 or E7 detected in less than 4% of healthy controls [75–77]. The identification of HPV association is clinically important, as the recommended therapy will be partially determined by HPV exposure, and HPV-OPC patients have a better prognosis than non-HPV-associated OPC patients [74].

Here, we focus on using the PCEF assay platform to detect anti-E7 IgG antibodies in both spiked serum samples and clinical samples with unknown anti-E7 antibody concentration to demonstrate the automation of PCEF detection

©2018 IEEE. Adapted, with permission, from C.M. Race *et al.*, “An automated microfluidic assay for photonic crystal enhanced detection and analysis of an antiviral antibody cancer biomarker in serum,” *IEEE Sensors Journal*, Vol. 18, No. 4, pp. 1464-1473, February 2018.

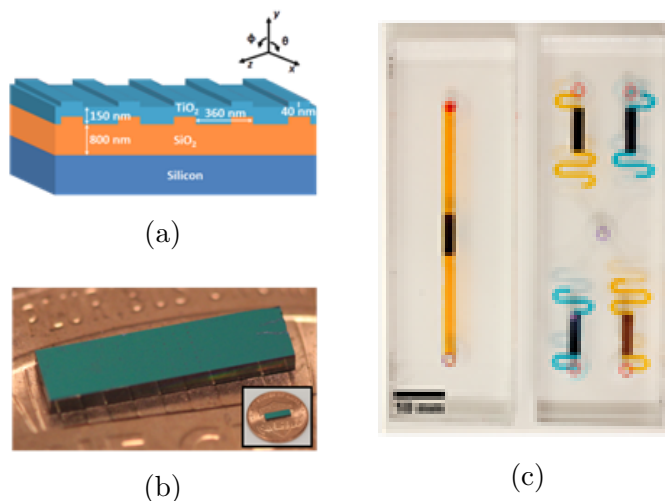


Fig. 2.1. (a) Schematic of the photonic crystal (PC) structure, composed of a high refractive index (RI) TiO_2 layer and low RI SiO_2 layer on a silicon substrate. (b) A $2\text{ mm} \times 8\text{ mm}$ PC with some visible printed protein spots on a penny for size comparison. (c) Photo of the PC-integrated single- (left) and four-channel (right) cartridges, with food coloring to indicate sample flow channel. Sample is introduced through the sample inlet holes, at the outside edges of the PCs. In the four-channel cartridge, the center hole serves as the common inlet for reagents once connected to the automated flow system.

and analysis. Our publication also considers this platform to demonstrate its potential for use in clinical diagnostic applications, but that discussion is beyond the scope of this work [78].

PCs are comprised of a periodically modulated surface of alternating high and low refractive index (RI) materials (Fig. 2.1a). The PCs used in this work consist of a low RI silicon dioxide (SiO_2) sub-wavelength, one-dimensional grating structure coated with a high RI titanium dioxide (TiO_2) layer, as described previously [79] and in the Methods section. With the correct combination of incident wavelength and angle, the “on-resonance” condition is fulfilled and a standing wave is generated within the TiO_2 layer of the PC that extends, in the form of an evanescent field, into the surrounding media (such as air) above the PC surface. Satisfying the boundary conditions derived from Maxwell’s equations, the evanescent field magnitude decays exponentially with increased distance from the surface of the PC.

The resonant electromagnetic coupling between light and the PC structure is the source of two enhancement mechanisms: enhanced excitation and enhanced extraction. The optical mechanisms behind PC enhanced excitation and

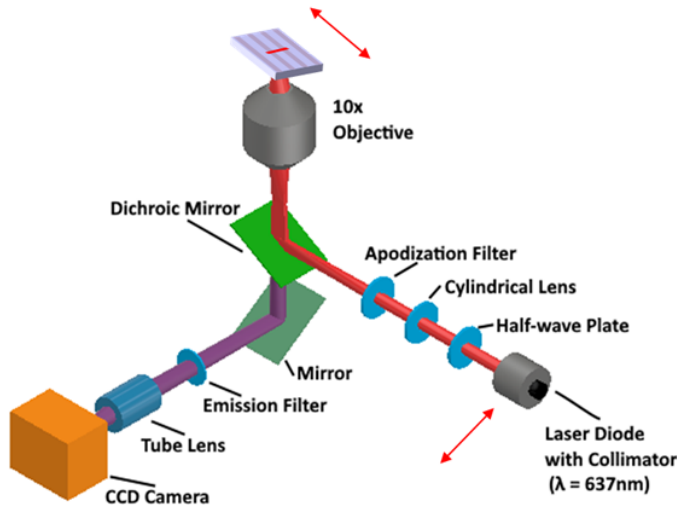


Fig. 2.2. Line scanner schematic. Both the laser diode and the sample are on motorized stages (with red arrows indicating direction of motion) that allow computerized control over the illumination angle and position.

enhanced extraction have been thoroughly described previously [10]. Briefly, the PC couples light from a collimated, monochromatic (laser) illumination source for a narrow range of incident angles, at which an electromagnetic standing wave is established in the TiO_2 layer of the PC with a magnitude that greatly exceeds the electric field intensity of the incident light. Through PC enhanced excitation, fluorescent dye molecules on the PC surface are exposed to greater electric field intensity than they would receive if they were on an ordinary glass surface. While a similar effect could be achieved by utilizing a more powerful laser, PC enhanced excitation achieves amplification of only surface-bound fluorophores (thus reducing background fluorescence) and enables the use of an inexpensive, low-power laser diode as the light source. PC enhanced extraction occurs for any photon emitter with a wavelength that approximately matches the wavelength of a resonant mode of the PC. While fluorescence emission on a glass substrate ordinarily radiates in all directions, the enhanced extraction effect directs emission normal to the PC surface, enabling the detection optics to collect a greater proportion ($5 - 10\times$) of all emitted photons. The PCs used in this work, in conjunction with the laser scanning detection instrument, take advantage of both effects. The combination of the two effects results in PC enhanced fluorescence (PCEF), with enhancement up to $8000\times$ at the PC surface [7]. Importantly, the detection instrument [7, 80] (Fig. 2.2) incorporates a motorized stage which enables tuning of the incident laser to its optimal “on-resonance” angle, at which the greatest enhanced excitation effect occurs.

Previous publications on the topic of PCEF for protein microarray applications have demonstrated the design and fabrication of silicon-based PCs [7, 79, 81, 82], a laser-scanning detection instrument with manual on-resonance adjustment [80], 3D-printed (via stereolithography) single-sample microfluidic cartridge and automated microfluidic control [82], and printed capture antibodies. The goal of this chapter involves the implementation of several modifications to make the technology platform compatible with a point-of-care testing environment, in which we envision a desktop instrument with a cost of less than \$10K that could be utilized by trained technicians in a health clinic. Ideally, the PCs must be embedded in a low-cost, easily manufacturable, single-use disposable cartridge into which the user introduces a single droplet of serum. The cartridge is inserted into an assay automation station containing reservoirs of two reagents (wash buffer and fluorophore-labeled secondary antibody). Due to the length of time required for the incubation steps of the assay, it is important to enable assays on independent test samples to be conducted simultaneously. Thus, cartridges allowing for the multiplexed testing of samples are desirable to facilitate these concurrent assays.

After the assay is complete (including automated drying of the PC surface), the cartridges are inserted into the laser-scanning detection instrument. Ideally, the user would have no interaction with the detection instrument other than to insert the cartridge and to initiate a scan. Therefore, mechanical alignment of the microarray to the scanned field of view, adjustment of the laser scanning instrument for optimal “on-resonance” illumination, determination of fluorescent spot intensities, and checking of internal controls for a valid test must all be performed automatically. The combined capabilities reported here represent a substantial engineering improvement that advances PCEF microarray technology from a labor-intensive laboratory capability toward a point-of-care automated technology.

2.2 Methods

2.2.1 Photonic Crystal Fabrication

The design and fabrication of silicon-based PCs used in this work has been described previously [7, 79]. Briefly, approximately 840 nm of low RI SiO₂

was deposited on an 8 in diameter Si wafer, followed by deep UV lithography and reactive ion etching to fabricate a 40 nm-deep grating with a period of 360 nm and 36% duty cycle (Novati Technologies Inc.). Next, a 150 nm thick, high RI TiO_2 layer was applied to the wafer by sputter deposition (Intlvac Inc.), resulting in the final device schematized in Fig. 2.1a. The wafer was subsequently diced into $2\text{ mm} \times 8\text{ mm}$ pieces (Fig. 2.1b) for incorporation within the single-channel or four-channel microfluidic cartridges (Fig. 2.1c). Fabrication upon 8 in diameter silicon wafers using tools and methods that are conventional for integrated circuit manufacturing assures a high degree of intra-PC uniformity and a high degree of reproducibility between independent PCs within a wafer and between wafers. All PCs have a resonant wavelength near 628 nm, with a bandwidth of $\sim 2\text{ nm}$, and a resonant reflection efficiency of $\sim 80\%$. The devices are designed for utilization in air, and resonant reflection spectra have been reported previously [7].

2.2.2 Line Scanner

Using the custom line scanning instrument (Fig. 2.2) [80], the first step of the detection process is to scan the surface of the PC to capture images of the fluorescently tagged protein spots (Fig. 2.3a). Importantly, the instrument is able to precisely adjust the incident angle of the laser illumination via motor-controlled linear translation of the distal end of the optical fiber that supplies light to the PC. The focal point of the cylindrical lens is at the back focal plane of the objective lens, so linear translation of the fiber tip results in modulation of the angle of light incident on the PC surface. In the system, 500 μm linear translation of the fiber end results in an approximately 1.59° modulation of the angle of incidence, and the angle can be controlled with 0.025° accuracy. The first step of the scanning process is to find the resonant angle of the PC within the E7 spots. Due to the mass density of the proteins printed and bound to the surface, the resonance angle of the PC is shifted by up to 2° between the silanized PC surface and the areas containing fluorescently tagged molecules, as shown in Fig. 2.4. To account for the additional resonance angle shift after binding of the anti-E7 and secondary antibodies, it is critical to measure the resonance angle of the E7 spots by scanning the angle from 0° to 8° to determine the angle at which maximum fluorescence intensity is emitted

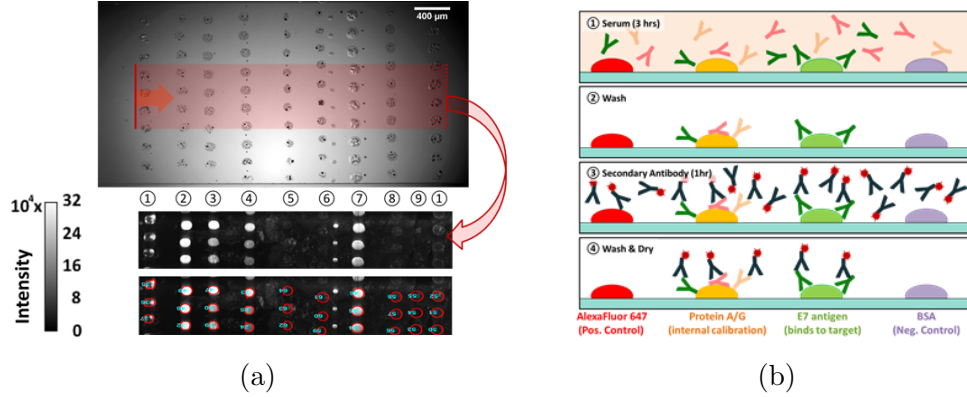


Fig. 2.3. (a) (top) Bright-field microscope image of protein microarray, where the red region corresponds to the area scanned with the line scanner, with the vertical laser line moving in the direction of the red arrow. (middle) Fluorescence intensity image obtained using the PCEF laser line scanner. (bottom) Result of the automated spot-finding algorithm. (b) Schematic of fluorescence-linked immunosorbent assay (FLISA). Figure courtesy of Lydia Kwon.

from the E7 spots on the PC. Spots near the edge of the PC are used for this on-resonance-angle-finding procedure so as not to photobleach the spots that will be scanned for analysis and quantification.

After the on-resonance angle is recorded, the sample stage is translated to an unscanned area of the chip to perform an on-resonance scan followed by an off-resonance scan (at an incident angle of 8°). On- and off-resonance scans are performed at the same location, across the length of the printed spots on the PC surface, to estimate the enhancement factor for the enhanced excitation mechanism. The pixel size of the CCD camera is approximately $1.6\ \mu\text{m} \times 1.6\ \mu\text{m}$, so images are gathered at $2\ \mu\text{m}$ increments in the direction perpendicular to the laser line. A sliding window algorithm is used to combine the line-scanned images together to form a fluorescence intensity image of the surface. For the sliding window algorithm, the fluorescence intensities of 5 consecutive scan lines are added together for each location on the surface. In other words, although the pixel width in the scan direction is only $2\ \mu\text{m}$, the computer captures a $10\ \mu\text{m}$ image to get fluorescence information for 2 pixels away from the center in either direction. This ensures that the result is the best estimate of fluorescence output due to the Gaussian intensity distribution of the laser intensity in the direction perpendicular to the scanning line.

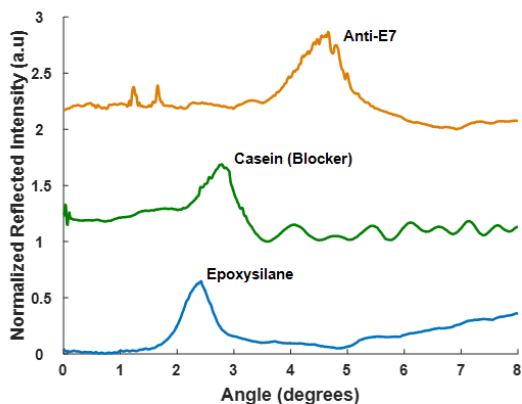


Fig. 2.4. Reflection spectrum of PC coated with: epoxy silane (blue), casein (green), and anti-E7 (orange).

2.2.3 Apodization Filter

The line scanning system incorporates an apodization filter in the optical path after the cylindrical lens, as shown in Fig. 2.2. The laser line has a Gaussian profile as measured along the length of the scan line, which results in non-uniform illumination of the fluorescent spots across the width of the chip. Spots in the center of the line receive approximately $2\times$ greater intensity than spots displaced only $200\ \mu\text{m}$ from the center. The consequence of this non-uniform illumination is a large standard deviation of spot intensities of replicate assay spots. An apodization filter partially attenuates the center of the scan line, resulting in more uniform illumination and ensuring that the fluorescence intensity at the line edge is similar to the fluorescence intensity at the center (Fig. 2.5a). The apodization filter was fabricated by depositing a thin layer ($\sim 12\ \text{nm}$) of gold, 4 mm in diameter, at the center of an optically transparent glass plate (Fig. 2.5b).

2.2.4 Automated Data Analysis

To perform data analysis on the fluorescence intensity images, I have implemented an automated algorithm to find and analyze the spots with minimal user input (Fig. 2.3a(bottom)). The algorithm uses Bernsen filtering and watershedding to identify local differences in intensity and to separate any unintended “satellite spots” (smaller, residue spots formed when more than one droplet is expelled from the printer tip during protein microarray printing) from the main printed protein spots [83]. Spots are also filtered by size and shape to exclude non-elliptical objects and background artifacts. This algorithm takes

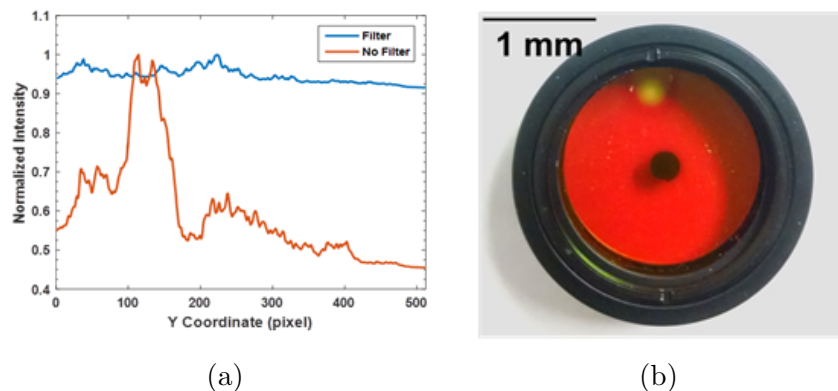


Fig. 2.5. (a) Comparison of laser line profile on bare PC before (orange) and after (blue) integration of apodization filter. (b) Photo of apodization filter.

as input raw fluorescent intensity data and outputs spot statistics, including spot median intensity, standard deviation, and average intensity of each column of spots. Each column of spots represents the positive control, negative control, experimental control, or biomarker.

After manual selection of a representative blank area of the PC for the background region, the algorithm subtracts the median intensity of the background spot from the median intensity of the corresponding protein spot, thereby accounting for vertical variations in the PC or in the laser line illumination. This method provides minimum covariance between spots, compared to other statistical analysis methods (e.g., excluding background subtraction, average spot intensity, or maximum spot intensity) [84]. By averaging each background-subtracted spot column, the algorithm computes enhanced excitation factor, which is defined as the on-resonance intensity divided by the off-resonance intensity of each assay column, providing insight into how accurately the on-resonance angle has been determined.

2.3 Results and Discussion

To validate the new method of finding the on-resonance angle, semiconductor quantum dots (QDs) from the Smith lab were used to quantify the output intensity at incremental deviations from the optimal resonance angle. QDs do not photobleach as quickly as organic fluorophores [85], enabling repeated scanning of the PC with a relatively stable emitted light intensity between

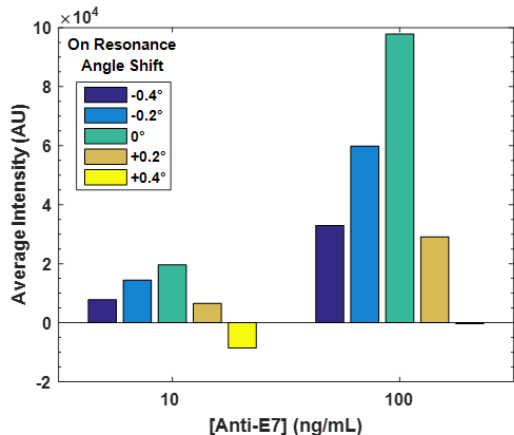


Fig. 2.6. Illustration of QD-tagged spot intensities (background subtracted) at different angles of illumination with respect to the resonance angle. Note that both samples exhibit highest intensity at the resonance angle.

subsequent scans. Because the 637 nm wavelength laser in the scanning setup is not optimal for typical QDs, the Smith lab provided alloyed (core)shell ($\text{Hg}_x\text{Cd}_{1-x}\text{Se}$) $\text{Cd}_y\text{Zn}_{1-y}\text{S}$ QDs [86] which exhibit enhanced excitation efficiency in the red and detectable emission at 685 nm. The on-resonance angle was obtained for different concentrations of the anti-E7 antibody and the fluorescence intensity was measured at angles near the on-resonance angle (Fig. 2.6). The background-subtracted QD intensity is always maximized at the on-resonance angle, with the intensity decreasing as the incident angle deviates from the resonance condition. While intensity is largest at the resonance condition, the decay on either side is asymmetric. This discrepancy can be explained by the order in which these scans at different angles were performed, as the QDs gradually photobleach (significant decrease in intensity could not be detected after 3 min of continuous illumination) [87]. The PCs were first scanned at the on-resonance condition, followed by -0.2° , then 0.2° , then -0.4° , and finally 0.4° away from the on-resonance condition.

As described in the Methods section, an automated spot-finding and analysis algorithm was implemented to reduce both data analysis time and user bias. The most notable improvement was in the time spent on data analysis, which improved up to 10-fold (approximately 30 min per chip) compared to finding spots and calculating average intensities manually. Furthermore, this method was used to thoroughly evaluate different analysis methods of calculating spot intensities (such as average, median, or maximum, all with or without background subtraction) that minimized covariance between different spots of the same biomolecule. The algorithm ensures that all spots are analyzed in the same manner and that comparison between different data sets is statistically

valid. Other groups have generated spot-finding algorithms [88], but this one is specifically applicable for fluorescence assays because it includes distinguishing main spots from satellite spots and accounts for non-uniformity in spot size, location, and spacing on the PC surface.

To use the PCEF platform for detection of anti-E7, a biomarker for HPV-associated OPC, we completed assays for a total of 40 clinical samples (gathered from 20 OPC patients and 20 healthy controls) at both on- and off-resonance. Conventional ELISAs were run concurrently on aliquots of the same samples by the Demirci Lab (Stanford University) [89]. The goal was to evaluate the diagnostic capability of PCEF platform to provide positive/negative discrimination of the presence of anti-E7 antibody, rather than to assess the clinical relevance of the antigen-antibody interaction of protein E7 and anti-E7 antibody in OPC patients. Therefore, the ELISA—an established diagnostic method—was chosen as the gold standard reference.

Figure 2.7 shows the off- and on-resonance E7 spot images obtained with PCEF, compared to the ELISA results and OPC status of select samples. Samples 1 and 2 represent those samples in which both the off- and on-resonance results correlated with both the ELISA and OPC status. Samples 3 through 9 represent samples in which there were discrepancies between the quantitative PCEF results and the ELISA status. More specifically, samples 3 through 5 indicate instances where at least one PCEF result (off- or on-resonance) was positive for an ELISA-negative sample. Meanwhile, samples 6 through 9 represent cases in which at least one PCEF result was negative for an ELISA-positive sample. Sample 9 is the one case in which both PCEF results were negative for an ELISA-positive sample.

While the assay did not compare perfectly to ELISA, there are promising results. Most notably, the enhancement factor (on-resonance intensity vs. off-resonance intensity) typically ranged from 10 – 25 \times , with some enhancement factors being as large as 200 \times . This means that the angle-finding method worked well on a variety of samples with different densities. There were two main issues: on-resonance spots being too bright for a “negative” result, and high background noise such that visible spots are considered “negative.” Both of these can be partially attributed to non-specific binding: the blocking agent (to prevent non-specific binding) did not work as well as it could have, potentially interfering with the data. These are improvements to be made

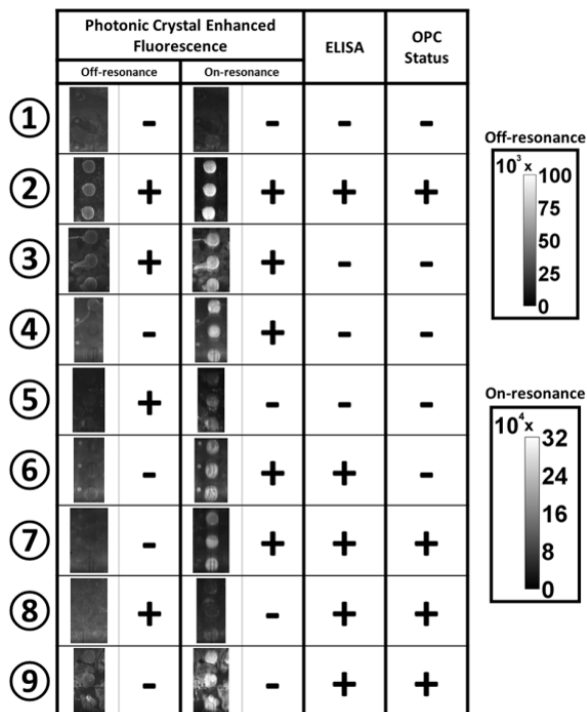


Fig. 2.7. PCEF results at off- and on-resonance, compared to ELISA results and OPC status for select samples, ① through ⑨, representing different variations in agreement between PCEF and ELISA results. Figure courtesy of Lydia Kwon.

before performing the next assay. We can also improve the calculation of background spot intensity for noisy assays in the data analysis software.

2.4 Conclusion

In this chapter, I have described methods for automating scanning and detection of oropharyngeal biomarkers using photonic crystal enhanced fluorescence. Data analysis time has significantly decreased without increasing errors made. The line scanning and data analysis system were first applied here to protein biomarkers for OPC. The accuracy in finding the “on-resonance” angle was improved and a method for automatically detecting fluorescence spot location on the PC surface, independent of location or brightness, was implemented. These methods are not specific to OPC and can be applied to future assays done using PCEF.

CHAPTER 3

A NEW SYSTEM FOR EXCITATION AND DETECTION OF QUANTUM DOTS USING PHOTONIC CRYSTALS

3.1 Introduction

Quantum dots (QDs) are becoming common alternatives to fluorophores in labeling and detecting biomolecules for live cell imaging [90–92], assays [93–96], and *in vivo* work [97–99]. The ability to design the size and composition of QDs in order to vary emission wavelength and intensity properties is highly desirable for these biological applications. Their resistance to photobleaching, broad excitation spectra, and high quantum-yield also make them much more efficient and easier to work with than traditional fluorescent dye molecules [92].

The Cunningham group has done previous work integrating QDs into 2D photonic crystals (PCs) for enhancing laser excitation and quantum dot emission [100–103]. The QDs embedded in these PCs undergo the Purcell effect, where the spontaneous emission rate of the QD is enhanced when coupled to a resonant cavity [104, 105]. The downside to this approach is that PCs have to be designed for the emission wavelength of each QD used. This becomes difficult for biological applications where multiplexing is desired or where QDs cannot be precisely placed on the surface for maximum enhancement.

I introduce the design of PCs to instead enhance the QD excitation, which is uniform for all emission wavelengths [86]. This approach will also enhance the emission of the QDs with the advantage that multiplexed detection can be performed with a combination of QD emission wavelengths and output intensities [103]. The emission wavelength in the QDs is sufficiently far away from the excitation wavelength (>100 nm) such that the absorption of the PC will not inhibit the decay rate, as it does for slightly decoupled QDs [104, 105]. In this work, I will detail the design and simulation of this new PC

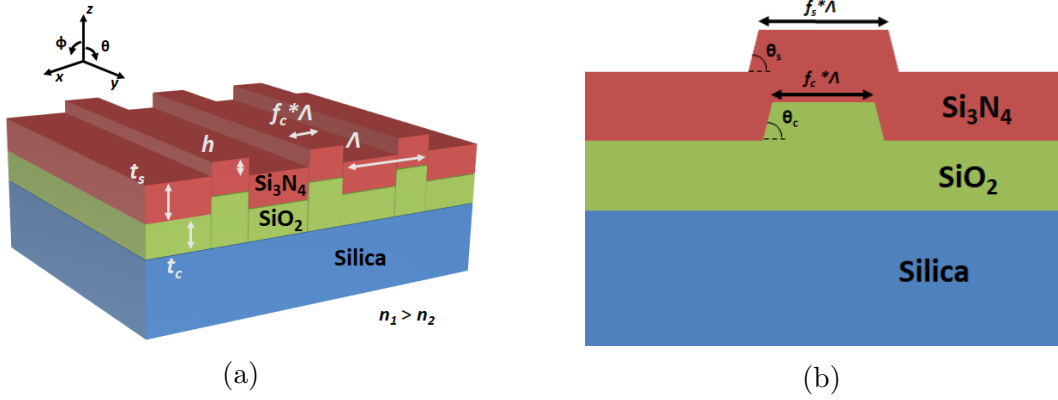


Fig. 3.1. (a) Ideal 1D PC with parameters corresponding to those in Table 3.1. $n_1 = n_{\text{Si}_3\text{N}_4}$ and $n_2 = n_{\text{SiO}_2}$. Not to scale. (b) One period xz slice of PC shown in (a) including non-normal sidewall angles and mismatched duty cycles that occur during fabrication.

and corresponding optical system to couple incident blue laser light to QDs for multiplexed biomarker detection.

3.2 Device Structure

3.2.1 Photonic Crystals for Enhancement of Quantum Dots

Here, I describe the design and simulation of PCs that enhance the excitation of QDs. These QDs are designed output uniform intensity light when excited under the same conditions, even at different emission wavelengths [86]. Since our collaborators in the Smith group plan to use multiple types of QDs for multiplexed detection, PCs can only be designed to enhance QD excitation, not emission. As mentioned previously, this is sufficient to enhance QD output.

The initial design was based off previous PCs designed for fluorophore excitation at $\lambda = 637 \text{ nm}$ [7]. I began by scaling the parameters, shown in Fig. 3.1a-b and described in Table 3.1, by the wavelength ratio between the lasers used to excite the PC resonance ($\frac{450 \text{ nm}}{637 \text{ nm}}$). After initial 2D simulations using Rigorous Coupled Wave Analysis (RCWA) (DIFFRACTMOD, RSoft), I iteratively optimized the parameters for maximum diffraction efficiency and enhancement for TM plane-wave illumination at λ and ϕ as defined in Fig. 3.1a. These results are shown in Fig. 3.2a-b. First, I optimized the slab (Si_3N_4)

Table 3.1. Device parameters for PCs depicted in Fig. 3.1a-b.

Symbol	Parameter	Value
Λ	Period [nm]	295
t_s	Si ₃ N ₄ Thickness [nm]	112
t_c	SiO ₂ Thickness [nm]	0
h	Grating Depth [nm]	28.1
f_c	Duty Cycle [%]	38.5
f_s	Si ₃ N ₄ Fill Factor [%]	$1.3 \times f_c$
θ_c	SiO ₂ Side Wall Angle [°]	82
θ_s	Si ₃ N ₄ Side Wall Angle [°]	78

thickness, which changes the linewidth and position of the resonance. Next, I adjusted the period, which shifts the resonance wavelength. Then I iteratively optimized the duty cycle and the grating depth, both of which vary the symmetry and linewidth of the resonance. For previous PC designs, the final step was to optimize the cavity (SiO₂) thickness, which shifts the Fabry-Perot background in the cavity and changes the enhancement factor (on-resonance, where λ, ϕ match the coupling conditions, vs. off-resonance, where λ, ϕ do not match the coupling conditions). In those cases, the resonance peak should be as close as possible to the Fabry-Perot minimum. However, in this case, the Fabry-Perot background is minimized due to the use of a fused silica substrate, as the refractive indices (RIs) of fused silica and SiO₂ are almost identical. Thus, for ease of fabrication, the cavity height is set to zero.

During these iterations, I used the diffraction efficiency vs. launch angle (ϕ) simulation (Fig. 3.2b) to ensure that there is enough margin to achieve resonance at some ϕ when the RI on the surface changes as the result of an assay. The final design is a trade-off between maximum enhancement and process capabilities. As an example, linewidth decreases, meaning Q-factor increases, for decreased grating depth. However, etching only a small grating depth, such as 15 nm, is difficult to reliably achieve. The linewidth at a grating depth of 35 nm is not much larger, and diffraction efficiencies at depths of 35 ± 10 nm are within 10%, providing a good compromise. The final electric field simulations are shown in Fig. 3.3a-b for off- and on-resonance conditions. The enhancement factor is $\sim 50\times$ at 100 nm above the surface, which is comparable to the previous PCs resonant at 637 nm.

PCs resonant at $\lambda = 450$ nm are being fabricated at Moxtek, a commercial producer of optical polarizers and beamsplitters. The non-proprietary fabrica-

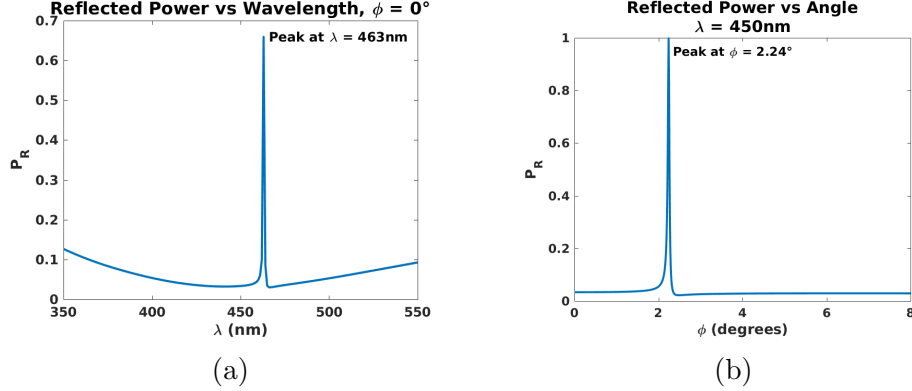


Fig. 3.2. Diffraction efficiency vs. (a) wavelength ($\phi = 0^\circ$) and (b) angle ($\lambda = 450$ nm) for an ideal PC. Labels on the graph specify the resonance peaks.

tion details are as follows. For fabricating the 1D grating, a photoresist pattern is transferred through an organic anti-reflective coating layer, which is first used to make a thin (~ 50 nm) Al hard mask. The Al mask is then used for etching (via RIE) a 28.1 nm grating into the SiO_2 cavity layer. Finally, the Al is stripped off before Si_3N_4 deposition. Potential optimizations include a thicker Al hard mask, with the lines trimmed to a lower duty cycle, in order to achieve a 38.5% duty cycle in the final SiO_2 grating.

3.2.2 Line Scanner Upgrade

A schematic of the upgraded detection instrument is shown in Fig. 3.4a-b. The Cunningham group has previously published the system for detection of protein

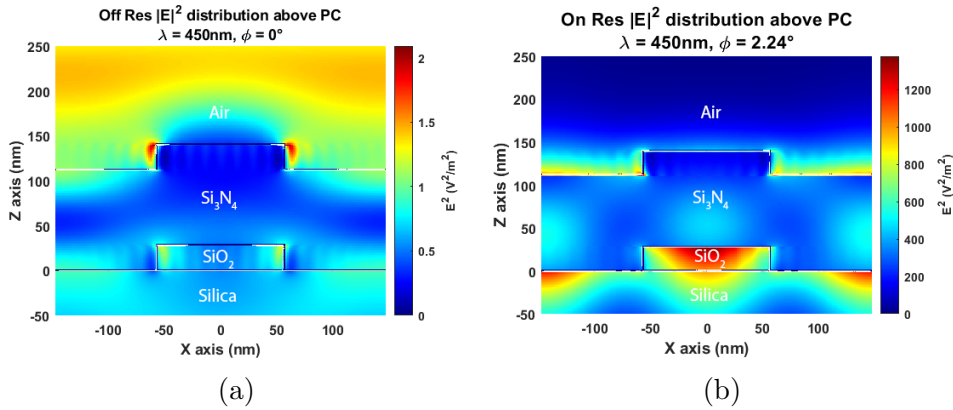


Fig. 3.3. (a) Off- and (b) on-resonance simulations of ideal PC. The enhancement factor 100 nm above the surface is $\sim 50\times$.

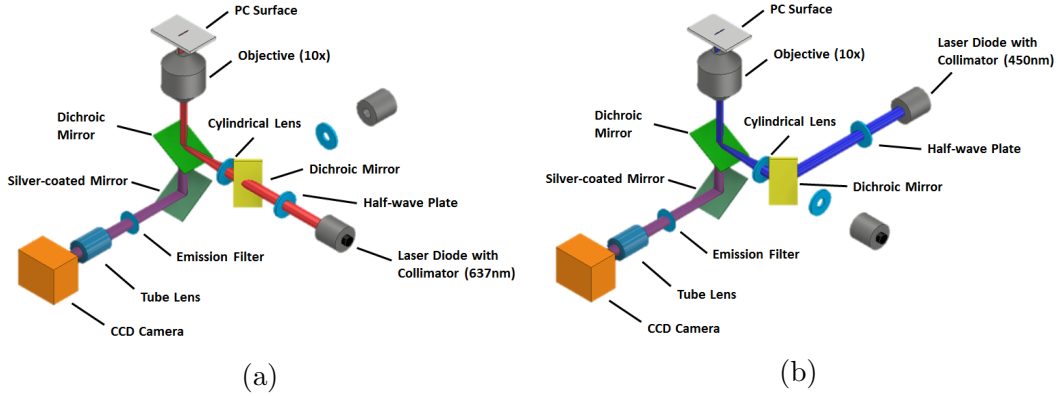


Fig. 3.4. Upgraded line scanner model for (a) the red laser path and (b) the blue laser path. The output beam is shown in purple.

and micro RNA cancer biomarkers [7]. Here, I have added an additional arm for the blue laser (Fig. 3.4b) as well as upgraded and realigned all the components to ensure proper focus and magnification. The illumination of this system consists of two laser diodes. The red arm contains a 70 mW solid-state laser (AlGaInP) at $\lambda = 637$ nm, while the blue arm contains an 80 mW solid-state laser (InGaN) at $\lambda = 450$ nm. Before joining paths, each laser passes through a half-wave plate in order to rotate its polarization perpendicular to the grating on the PC surface. This ensures excitation is maximized. The dichroic mirror at the intersection of the laser paths serves to reflect the $\lambda = 450$ nm laser at a 90° angle while transmitting the $\lambda = 637$ nm beam. Then, both beams pass through a cylindrical lens ($f = 150$ mm), which focuses them onto the back focal plane of an infinity-corrected $10\times$ or $50\times$ objective (Olympus Plan N) such that a line is formed at the PC surface. A second dichroic mirror reflects the laser excitation onto the PC surface while passing the longer wavelength QD-emission onto the emission filter and tube lens ($f_{tl} = 200$ mm) that projects the fluorescence image onto the entrance slit of a Czerny-Turner spectrophotometer (Horiba iHR550). At the exit of the iHR550 is an EMCCD camera (Hamamatsu 9100C). In imaging configuration, the iHR550 turret rotates to a mirror, while in spectral configuration, the turret rotates to a $300 \ell/\text{mm}$ grating (600 nm blaze wavelength). Using the $10\times$ objective, the laser FWHM displayed on the EMCCD is $\sim 6 \mu\text{m}$.

The $\lambda = 637$ nm laser, half-wave plate, first dichroic mirror, and cylindrical lens are placed on a motorized linear stepping stage (Zaber LSM-25), movement of which results in a translation of the line focused laser on the back focal plane

Table 3.2. PCEF system parameters used to calculate resolution limits.

Symbol	Parameter	Value
f_{obj}	Focal length of 10× objective [mm]	18
f_{tl}	Focal length of tube lens [mm]	200
w_p	Pixel width/height [μm]	16
N_{pixel}	Number of pixels in CCD (1D)	512
m	Diffraction order	1
NA	Numerical aperture of 50× objective	0.5
d	Grating line spacing [$\mu\text{m}/\ell$]	3.33
w_s	Slit width [μm]	50
f_{spec}	Focal length of mirrors in Czerny-Turner setup [mm]	550
M_{CT}	Czerny-Turner magnification	1.1

of the objective, changing the incident angle in the ϕ direction. The PC is also on a motorized sample stage (MS2000, Applied Scientific Instruments) which translates in all 3 (x, y, z) directions to scan the sample surface (x, y) and to focus the laser (z).

While not precisely a 10× magnification system,

$$M = -\frac{f_{tl}}{f_{obj}} = -\frac{200}{18} \approx -11.1$$

the $f_{tl} = 200$ mm is necessary to in order to have sufficient space between all of the optical components.

3.2.3 System Resolution

Before taking experimental data, it is important to understand both spectral and spatial resolution limits on imaging capability due to the components of the PCEF system (parameters shown in Table 3.2). The spatial resolution is simpler to calculate, as it does not depend on the slit width (w_s) and grating line spacing (d). There are two components to spatial resolution: spacing limited by imaging wavelength and spacing resolved by the EMCCD. First, the spatial resolution limited by wavelength is:

$$\begin{aligned} r_\lambda &= \frac{\lambda}{2 * \text{NA}} \\ &= \frac{450 \text{ nm}}{2 * 0.5} = 450 \text{ nm} \end{aligned}$$

Thus, we cannot resolve features separated by less than 450 nm. Next, the spatial resolution limited by the EMCCD (calculated here for the 50× objective), which also determines the step size for scanning the laser line across the surface, for pixel width w_p and PCEF magnification M_{PCEF} is:

$$\begin{aligned} r_{\text{PCEF}} &= \frac{w_p}{M_{\text{PCEF}}} \\ &= \frac{w_p}{\frac{f_{\text{el}}}{f_{\text{obj}}/5}} \\ &= \frac{16 \mu\text{m}}{\frac{200 \text{mm}}{18 \text{mm}/5}} = 288 \text{ nm} \end{aligned}$$

Note that, with a 50× objective, the camera can image smaller features than can be resolved with visible light.

The spectral resolution of the system depends primarily on the characteristics on the Czerny-Turner setup, which are also listed in Table 3.2. The linear dispersion $\frac{dl}{d\lambda}$ of the spectrophotometer for the diffracted angle θ_d is [106]:

$$\frac{dl}{d\lambda} = f_{\text{spec}} \frac{m}{d} \frac{1}{\cos \theta_d}$$

where, for small θ_d , $\cos \theta_d \approx 1$. Assuming the image of the slit on the CCD $w'_s = M_{\text{CT}}w_s$ and that $w_s > w_p$, the full width half maximum (FWHM) of the spectrometer is:

$$\begin{aligned} \text{FWHM} &= \left(\frac{dl}{d\lambda} \right)^{-1} \max\{w'_s, w_p\} \\ &= \left(\frac{dl}{d\lambda} \right)^{-1} M_{\text{CT}}w_s \\ &= \frac{d}{mf_{\text{spec}}} M_{\text{CT}}w_s \\ &= \frac{3.33 \mu\text{m}/\ell}{1 * 550 \text{ mm}} * 1.1 * 50 \mu\text{m} = 0.333 \text{ nm} \end{aligned}$$

which means that the PCEF system can resolve spectral peaks that are at least 0.333 nm apart.

Both spatial and spectral information are combined on the EMCCD, as the PCEF scanning system generates a spectrum for each point on the laser line. There are thus different resolutions to consider in each of the final spectral

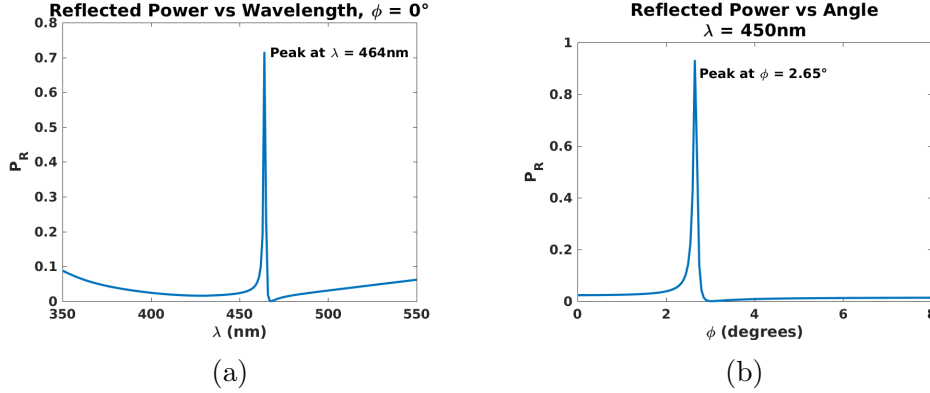


Fig. 3.5. Diffraction efficiency vs. (a) wavelength ($\phi = 0^\circ$) and (b) angle ($\lambda = 450$ nm) for an ideal PC with an $n = 1.4$ biomarker on the surface ($r = 50$ nm). Labels on the graph specify the resonance peaks.

images. The implications of this will be evident during the later discussion of QD scans.

3.3 Results and Discussion

Simulated results are shown for two cases: a biomarker on the surface, similar to detection during an assay, and imperfections that occur during fabrication. I also show experimental results for QDs conjugated to single-stranded DNA (ssDNA) on the PC surface.

3.3.1 Biomarker Simulation

Here, I used RCWA to simulate a biomarker as a sphere of radius $r = 50$ nm and RI $n = 1.4$ on top of the PC grating, with the same 2D simulation conditions specified previously (TM plane-wave illumination). Modeled reflection spectra vs. wavelength and incident angle are shown in Fig. 3.5a-b. There is $\sim 0.3^\circ$ increase in the on-resonance angle from the original model with no biomarker. This is similar to the incident angle shift that occurred in previous experiments with one molecule, such as silane, on the surface. However, depending on the surface treatment and assay conditions, there can be a much larger shift based on how many layers of molecules are present on the surface. The PC is designed so that the resonance angle increases with increased RI on the surface, and

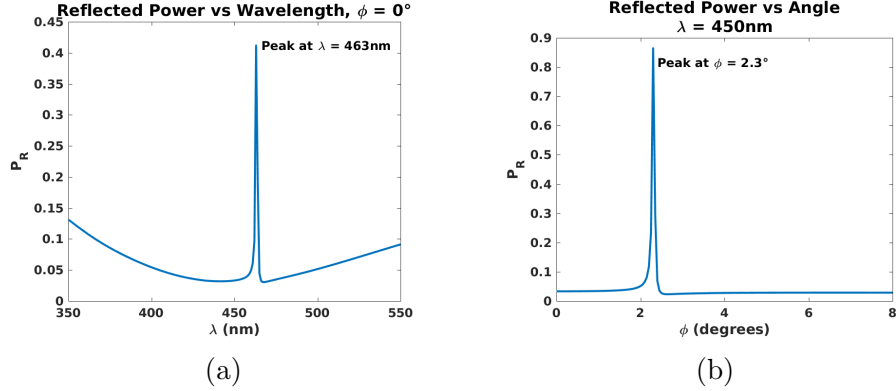


Fig. 3.6. Diffraction efficiency vs. (a) wavelength ($\phi = 0^\circ$) and (b) angle ($\lambda = 450$ nm) for PC with non-normal sidewalls and non-uniform duty cycles. Labels on the graph specify the resonance peaks.

there is sufficient margin in the detection system to accommodate incident angles up to 12° .

3.3.2 Non-Ideal Structure Simulations

Here, I used RCWA to simulate non-perpendicular sidewall angles, as listed in Table 3.1 and shown in Fig. 3.1b. Modeled reflection spectra vs. wavelength and incident angle are shown in Fig. 3.6a-b. There is $\sim 0.6^\circ$ increase in the on-resonance angle, an increase in linewidth, and a decrease in diffraction efficiency from the original model with normal sidewall angles. This is expected given that the sidewalls introduce higher diffraction orders such that the light can no longer be completely coupled into the structure. E^2 field distributions are shown for off- and on-resonance in Fig. 3.7a-b. The enhancement factor is $\sim 13\times$ at 100 nm above the surface, which is similar to the actual performance of the $\lambda = 637$ nm PCs.

3.3.3 Device Fabrication and Characterization

The devices were fabricated at Moxtek, a commercial company specializing in wire-grid polarizers, as described previously. Due to the small duty cycle and short grating height needed to maximize the resonance near $\lambda = 450$ nm, fabrication required many iterations and design changes to produce a decent yield. As shown in SEM images of Fig. 3.8a-b, there are both variations in

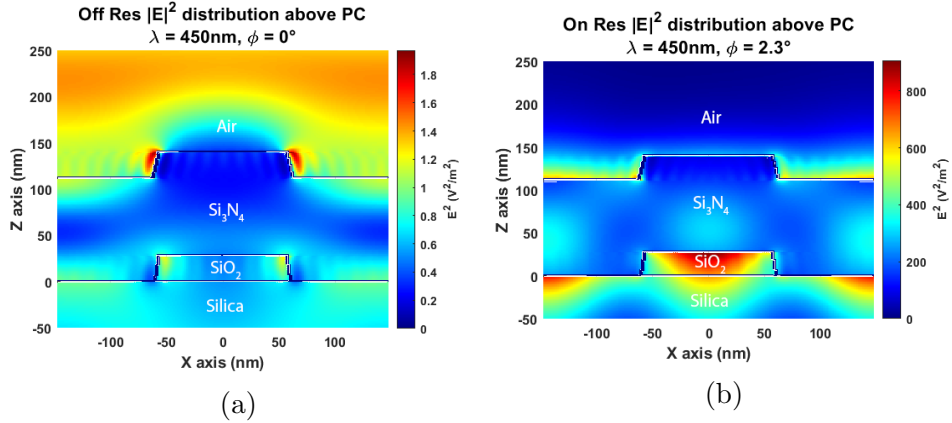
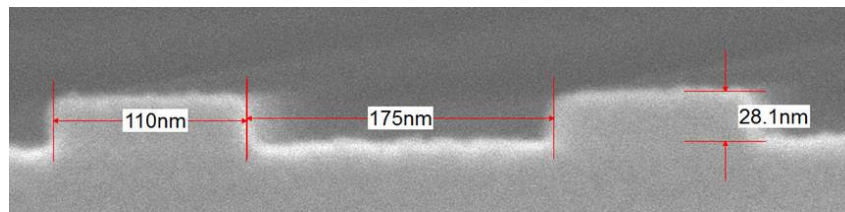


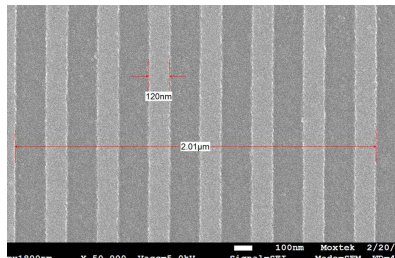
Fig. 3.7. (a) Off- and (b) on-resonance simulations of fabricated PC. The enhancement factor 100 nm above the surface is $\sim 13\times$.

grating height and surface roughness that contribute to an increased linewidth and lower quality factor than previous devices with a resonance peak near $\lambda = 637$ nm. With multiple design iterations, these inconsistencies were minimized and the fabrication yielded a higher number of functional devices. The angle-tuning ability of the PCEF system allows for a greater proportion of functional devices, as a slightly shifted resonance peak can be tuned appropriately using the instrument.

Figures 3.9a-b show measured PC spectra vs. wavelength and angle. To measure power vs. wavelength, light transmitted through the PC from a white light source (Ocean Optics DH-2000-BAL) is captured via a photodiode and



(a)



(b)

Fig. 3.8. (a) Cross-sectional and (b) bird's eye view of fabricated PCs.

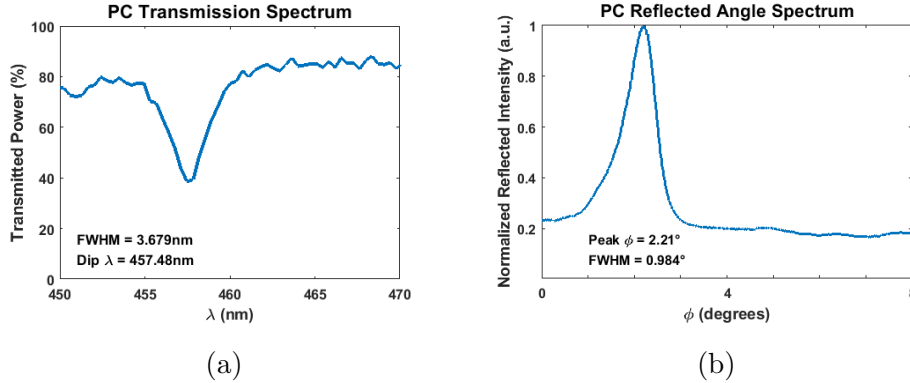


Fig. 3.9. (a) Transmission spectra and (b) peak reflected power angle spectrum for fabricated PCs.

coupled via an optical fiber into a spectrometer (Ocean Optics USB2000). To measure the reflected intensity vs. angle, I used the PCEF setup in Fig. 3.4b as described in Section 2.2.2. Briefly, the angle of the light incident on the surface is swept by translating a motorized stage, which focuses the laser at a different point on the back focal plane of the objective. During this process, the software captures images from the EMCCD camera at each step and computes the peak reflected intensity. The PCEF setup is calibrated such that the on-resonant angle corresponds to the wavelength dip found using the transmission setup.

3.3.4 Quantum Dot Fluorescence Scans

Before any testing, it is necessary to ensure that the surface of the PC is made biocompatible by sputtering ~ 10 nm of TiO_2 on the Si_3N_4 . In order to test the enhancement properties of the new PCs resonant near $\lambda = 450$ nm, I used commercially available QDs emitting at $\lambda = 655$ nm (Thermofisher QdotTM 655 Streptavidin Conjugate). Streptavidin on the QD binds to biotin on one end of the ssDNA (IDT 10mer DNA oligo), which is bound to the silanized (Sigma-Aldrich (3-Glycidyoxypropyl)trimethoxysilane) surface of the PC via an amine (Fig. 3.10). Absorption/emission spectra of QDs are shown in Fig. 3.11. Our $\lambda = 450$ nm excitation laser is well within the range of excitation for the QDs, as standard microscopes typically use a $\lambda = 488$ nm laser.

The first test was to validate QD enhancement. For this test, a high concentration of QDs were dried on the surface. Using the method described in Section 3.3.3, I found the angle at which peak reflection occurred for the

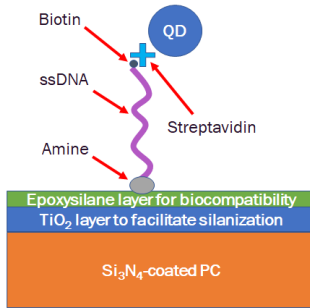


Fig. 3.10. Surface chemistry of QD-conjugated ssDNA on PC. Not to scale.

QD-coated PC (5.75°), completed a line scan (“on resonance”), and repeated the procedure for normally incident light (“off resonance”). These results are shown in Fig. 3.12, where the average enhancement factor is $\sim 5.5\times$. Note that this enhancement is smaller than the predicted $13\times$. This is due to the actual PC having an increased linewidth as a result of surface roughness and other imperfections not accounted for in the simulated model.

After verification of enhancement, I performed line scans, using the system described in Section 3.2.2, of the PC surface with different concentrations of QDs bound to ssDNA. It is important to note that the surface is covered with ssDNA, so the limiting factor is the concentration of QDs, as each QD should bind to ~ 1 ssDNA. The QD-streptavidin conjugates are only ~ 20 nm in diameter, thus they are diffraction-limited at visible wavelengths. As they cannot be identified by size alone, single QDs are typically distinguished by their characteristic blinking [107–109]. We did not see any such blinking while observing QD output in real-time on the EMCCD camera, leading to the conclusion that either the QDs are too highly concentrated to resolve or they aggregated in solution. Future work is planned to explore these possibilities. We verified that the emission was from QDs, rather than artifacts, using spectral scans, discussed further in Section 5.2.2 and shown in Fig. 5.3a-c, that display the signature QD Gaussian emission centered at ~ 655 nm.

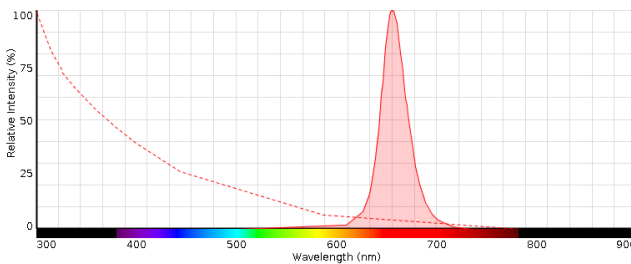


Fig. 3.11. Absorption/emission spectra of Thermofisher Qdot™ 655 streptavidin conjugate.

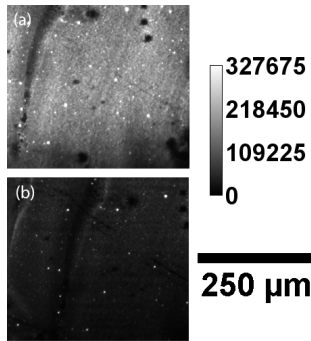


Fig. 3.12. (a) On resonance and (b) off resonance scans of PCs coated with QD-conjugated ssDNA.

In Chapter 2, I performed scans of a dry surface, during which samples were scanned upside down and light was reflected off of the PC surface back into the objective (Fig. 3.4b). In this case, due to surface chemistry complications drying the DNA/QD conjugate, I performed scans of the QDs in solution, right side up, contained on the PC surface in ~ 5 mm PDMS wells. As shown in Fig. 3.13, there is enough margin in the PC design and the PCEF system to accommodate the larger angle shift due to the increased RI on the surface of the QD solution vs. air. It is important to note that, although extra QDs are in solution, only the ones bound to DNA are visible because of the height of the evanescent field on the PC. The QD aggregates are clearly visible in Fig. 3.14a-c, but they are slightly more blurry than dry surfaces as a result of the long working distance, low-NA objective directing the light through the PC and back during each scan. Regardless of the blurriness of the image, it appears that each $10\times$ decrease in concentration correlates to $\sim 10\times$ decrease in the number of spots that can be physically counted on the surface. This leads to high confidence in our system to both enhance QD emission and produce valid results over a wide range of QD-labeled biomarker concentrations.

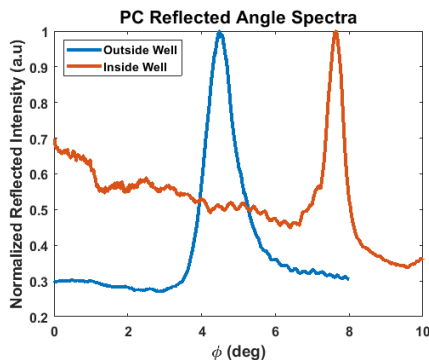


Fig. 3.13. Angle scans of PC inside and outside of the PDMS well containing QD solution. The surface of the PC outside the wells is only silanized - there is no ssDNA conjugated to it.

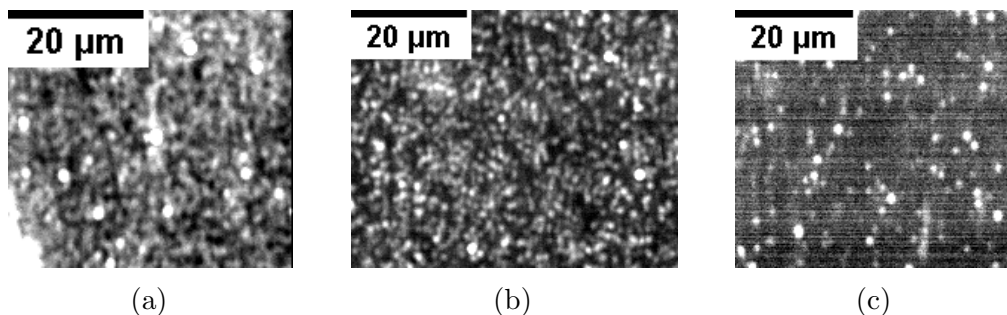


Fig. 3.14. QD normal incidence line scans at concentrations of (a) 1 nM, (b) 100 pM, and (c) 10 pM.

3.4 Conclusion and Future Work

In this chapter, I showed simulations and experimental data of a new PC to enhance 450 nm laser excitation for QDs and a redesigned optical system to detect multiplexed QD emission. The electric field is up to $13\times$ larger at the PC resonance and the line scanner system can now be used to excite both fluorophores (Cyanine-5) and QDs (at a variety of emission wavelengths from 525 nm to 685 nm), as demonstrated experimentally using 655 nm QDs. We plan to further investigate both the effects of using a low-NA objective and the optimization of surface chemistry to more clearly image QDs on the surface. We plan to use both the fluorescence imaging capability and the spectral imaging capability of the PCEF system in order to detect multiplexed QD-tagged ssDNA sequences. In future work, this system will be used to detect QDs conjugated to messenger RNA variants to evaluate treatment efficacy in metastatic castrate-resistant prostate cancer.

CHAPTER 4

THE APPLICATION OF HYPERBOLIC METAMATERIALS TO ENHANCE QUANTUM DOT-BASED BIOSENSORS

4.1 Introduction

Photon emitters are the cornerstone of technologies that include medical diagnostics, video display, digital communication, and lighting. Classes of emitters include phosphors, fluorescent chemical compounds, and semiconductor-based quantum dots (QDs), which are each excited by an external illumination source that stimulates emission at a specific wavelength. At the nanoscale, both efficient coupling of excitation energy into the emitter and selective channeling of its emission in a specific direction are key to obtaining optimal energy efficiency, which in turn impacts achievable limits of detection for sensing disease biomarkers, battery life of mobile devices, and power conversion efficiency of lighting.

By incorporating photon emitters into custom-engineered nanostructures, it is possible to substantially enhance the energy coupled into the nanostructures. Photonic crystal (PC) nanostructures represent one example, as, under a specific set of coupling conditions (a precise excitation wavelength and incident angle), PCs sustain a resonant electromagnetic standing wave, with an evanescent field extending beyond the surface that enhances the output of emitters within that evanescent field. This results in up to $100\times$ enhancement factor in excitation power for emitters on the PC surface. However, PC-based resonant energy enhancement has an important fundamental drawback: as the energy enhancement factor increases, the resonant energy coupling condition becomes more stringent, resulting in the need to precisely collimate and align the excitation source.

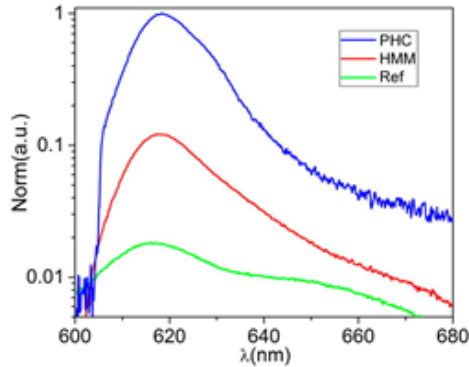


Fig. 4.1. Photoluminescence spectra of a flake of the 2D semiconductor WS₂ on the surface of a PHC, HMM, and Si with native oxide reference substrate. Reprinted with permission from [111]. ©2016 American Chemical Society.

A novel class of materials allow us to achieve high enhancement factors for photon emitters with far less stringent coupling conditions, resulting in energy coupling to photon emitters that is not only highly efficient, but also rugged enough for applications in which high mechanical stability and/or precise optical alignments are not possible. Man-made optical metamaterials are being explored for their unique properties in applications ranging from cloaking devices to perfect lenses. These structures, typically fabricated by depositing ultra-thin layers of alternating metals and dielectrics, allow engineering of the interaction between light and matter that is not possible with naturally occurring materials.

Metamaterials have been shown to provide unique field enhancement to slot waveguides and to yield extra sensitivity for plasmonic biosensing devices, supporting significant enhancement in metamaterial structures [71, 110]. Previously published reports have yet to fully explore the use of periodically structured metamaterials for enhancement of photon emitters (such as QDs) above the surface, as will be further explored and demonstrated here.

PCs using a metamaterial instead of a dielectric layer, called photonic hypercrystals (PHCs), have already been simulated in the infrared and microwave regimes, where they can provide near-perfect, although lossy, lensing from light at any incident angle, exhibiting an omnidirectional band gap [112]. They have also been shown to enhance photoluminescence from 2D semiconductor materials on the surface (Fig. 4.1) and have been made into perfect absorbers [111, 113]. Here, I demonstrate that PHC structures are capable of resonant electromagnetic coupling and enhancement over a large range of incident angles for a laser illumination source. This results in efficient coupling with and high enhancement of QDs for biosensing applications. My PHC design combines the

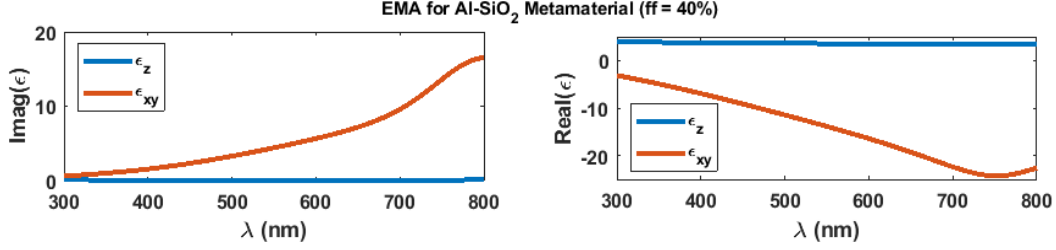


Fig. 4.2. Anisotropic permittivities calculated for the Al-SiO₂ HMM of Fig. 4.3a (fill factor = 40%) using the effective medium approximation (described in Section 4.2.3). $\Re\{\epsilon_{xy}\} < 0$ while $\Re\{\epsilon_z\} > 0$.

light engineering capabilities of PCs with the broadband enhancement effects of metamaterials.

4.2 Device Structure

Hyperbolic metamaterials (HMMs) are fabricated by layering alternating metal and dielectric materials [114]. They facilitate precise control of light propagation as a result of the conductivity differences between the materials: electrons flow freely across the metal surface, but not as easily between the layers, resulting in different permittivities in different directions. For a selected metal/dielectric combination, there are negative real permittivities (ϵ_r) in one or more orientations of the crystal, while permittivities in the perpendicular orientations remain positive, as shown in the example of Fig. 4.2. This is the defining feature of an HMM. The unique physics of HMMs also permit a wide variety of angles to couple into the structure, leading to broadband enhancement effects. This will be further explored in Section 4.3.2.

HMMs are integral for the fabrication of PHCs, first described by Narimanov in 2014 and shown in Fig. 4.3b-c [66]. A PHC consists of periodically structured regions that contain metallic or dielectric materials layered with HMMs. Like a PC, this periodicity can extend in 1-, 2-, or all 3-dimensions.

4.2.1 Simulations

I have fully designed and simulated a PHC structure using both commercially available finite difference time domain (FDTD) electromagnetic computer simulations (Lumerical) and rigorous coupled wave analysis (RCWA) for periodic

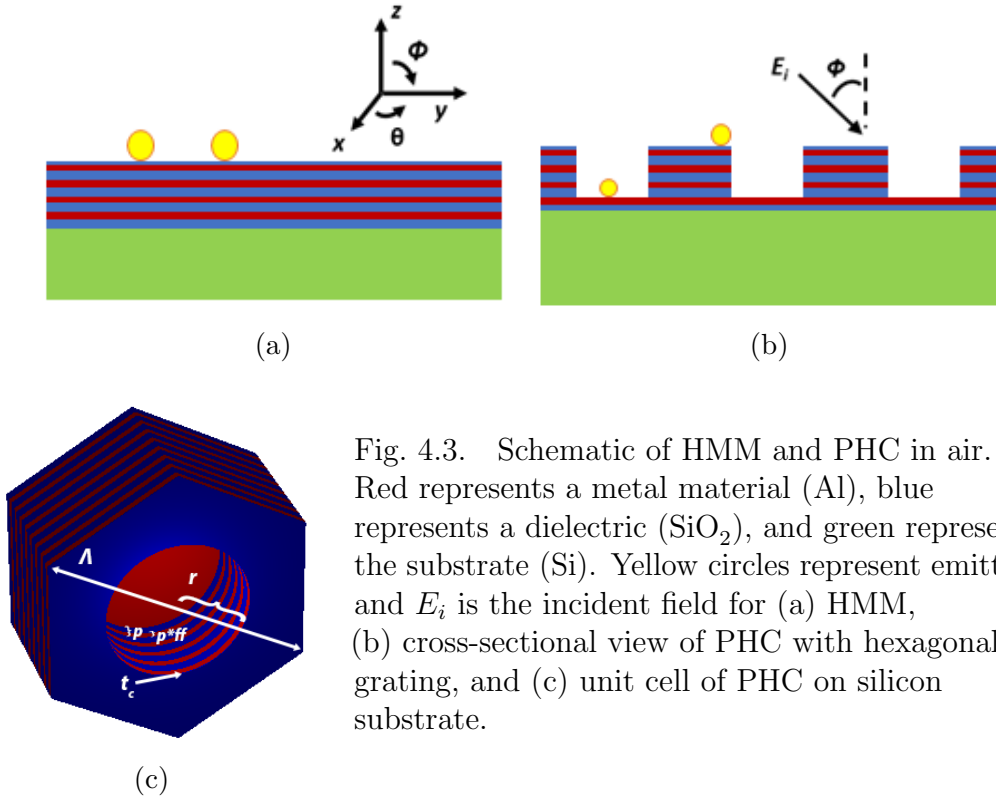


Fig. 4.3. Schematic of HMM and PHC in air. Red represents a metal material (Al), blue represents a dielectric (SiO_2), and green represents the substrate (Si). Yellow circles represent emitters and E_i is the incident field for (a) HMM, (b) cross-sectional view of PHC with hexagonal grating, and (c) unit cell of PHC on silicon substrate.

layered structures (S^4 [115]), exploring the effect of changing materials, device structure, and layer thicknesses of the hexagonal PHC depicted in Fig. 4.3c. Permittivity data for Al is from Brendel-Bormann model in Rakić *et al.*, while permittivity data for SiO_2 is experimentally obtained by our previous collaborators at Moxtek via ellipsometry [116]. Unless otherwise stated, simulations are done in 3D and incident light is a TM-polarized plane wave at normal incidence.

The combination of Al and SiO_2 was chosen to optimize device performance at 450 nm for compatibility with previous work detecting QDs (see Chapter 3). I specifically used Al (as opposed to Ag or Au, which are also commonly used for applications in the visible spectrum) because of its low plasma frequency ($\omega_p = \frac{2\pi c}{\lambda_p}$), or the frequency at which the real part of the permittivity (ϵ_r) crosses zero [117]. The ω_p values for Ag and Au are too close to $\lambda = 450$ nm to be able to form a metamaterial that extends sufficiently into the hyperbolic range to yield large electromagnetic enhancements [118, 119]. SiO_2 was chosen for its relative ease of fabrication and its ability, in combination with Al, to yield such a metamaterial based on the effective medium approximation described

Table 4.1. Device parameters for PHC depicted in Fig. 4.3c.

Symbol	Parameter	Value
Λ	Lattice constant [nm]	434
p	Vertical period [nm]	30
ff	Fill factor [%]	40
r	Etch radius [nm]	123
t_c	SiO ₂ cap thickness [nm]	2
N_p	Number of vertical periods	8
N_{etched}	Number of etched vertical periods	5

in Section 4.2.3. Other dielectrics, such as TiO₂ or Al₂O₃, have too large a permittivity or are too lossy at $\lambda = 450$ nm to be effective.

4.2.2 Optimization

Device optimization leads to a combination of an HMM (Al and SiO₂) and a dielectric (air) such that there exist broadband coupling conditions to the PHC for improved enhancement of QDs. The design described here is based on a structure by Galfsky *et al.* for a spontaneous emission enhancer and is shown in Fig. 4.3c [111].

In order to optimize the device for $\lambda = 450$ nm at $\theta = \phi = 0^\circ$, it is first important to ascertain the physical effect of varying different parameters of the PHC, which are shown in Table 4.1. The three most important factors in optimization are the fill factor, lattice constant, and hole radius, as shown in Fig. 4.4a-b. Before varying those, I set limits on the number of layers forming the HMM, the number of etched layers in hole, and the layer thicknesses. Theoretically, more layers of the HMM should yield a better performing device, in terms of minimizing non-local effects from the vertical period $p \ll \lambda$ [120]. Practically, the amount of absorption in the metal does not yield significantly increased performance (determined by simulations of reflected power vs. wavelength) for the number of periods $N_p > 8$. Similarly, the number of etched layers yields maximum performance at $N_{etched} = 5$. Etching exactly this distance during device fabrication will likely not be feasible, but it is sufficient for optimization purposes. Finally, the value of p has no effect on the device performance as long as it is significantly subwavelength. Here I set $p = 30$ nm $\ll 450$ nm for ease of fabrication while keeping the total structure height small.

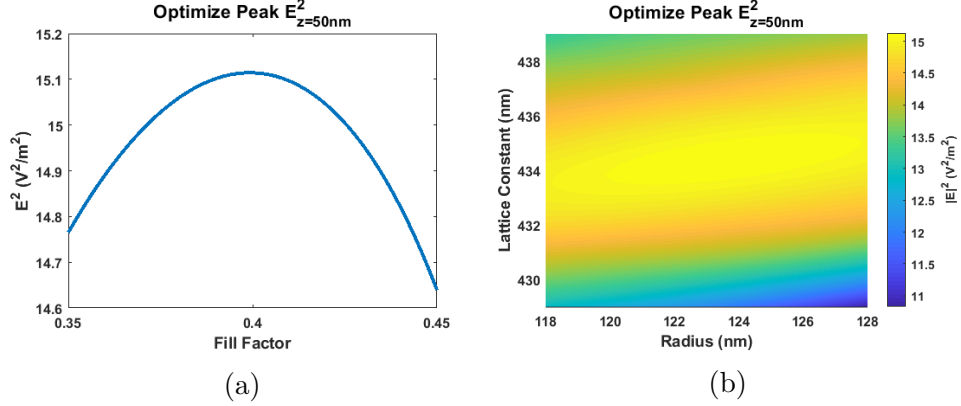


Fig. 4.4. Optimizing peak enhancement at 50 nm above the surface for the parameters of the PHC (a) fill factor and (b) hole radius and lattice constant.

After the relatively straightforward task of optimizing the HMM, I used S^4 to iterate through all combinations of fill factor (ff), lattice constant (Λ) and hole radius (r) to achieve the peak E^2 at $z = 50$ nm above the PHC surface. The height $z = 50$ nm was chosen because that is approximately the distance of the QD-conjugated single-stranded DNAs above the silanized surface for the experiments described in Chapter 3. The combination of Λ and r determine the wavelength at which the maximum enhancement occurs, as shown in Fig. 4.4b. The optimal $r \propto \Lambda$, but varying Λ has the larger effect. For optimizing the device for λ slightly greater (less) than 450 nm, given that all other factors remain the same, all that is needed is to increase (decrease) Λ while keeping r/Λ constant. Finally, varying ff (Fig. 4.4a) increases or decreases the value of E^2 , but does not spectrally shift the peak E^2 .

4.2.3 Effective Medium Response

Although I used computational methods to simulate the full response of the HMM, the effective medium approximation (EMA) allows for averaging the periodic layers into a metasurface with one effective permittivity ϵ^{eff} . The EMA applies for $\Lambda \ll \lambda = 2\pi/k_0$ [121]. For a transverse magnetic (TM) wave:

$$\epsilon^{\text{eff}} = \begin{bmatrix} \epsilon_{xy}^{\text{eff}} & 0 & 0 \\ 0 & \epsilon_{xy}^{\text{eff}} & 0 \\ 0 & 0 & \epsilon_z^{\text{eff}} \end{bmatrix}$$

The dispersion relation ($k_0 = 2\pi/\lambda = \omega_0/c$) for a TM wave is:

$$\frac{k_x^2}{\varepsilon_z^{\text{eff}}} + \frac{k_z^2}{\varepsilon_{xy}^{\text{eff}}} = k_0^2$$

And, finally, the EMA for the metal (ε_1)/dielectric (ε_2) structure with $f_1 = ff$ as the fill fraction of metal and $f_2 = (1 - ff)$ as the fill fraction of dielectric:

$$\varepsilon_{xy}^{\text{eff}} = \varepsilon_{xy}^{(0)} = \frac{\varepsilon_1 \varepsilon_2}{f_2 \varepsilon_1 + f_1 \varepsilon_2}$$

$$\varepsilon_z^{\text{eff}} = \varepsilon_z^{(0)} = f_1 \varepsilon_1 + f_2 \varepsilon_2$$

The EMA is not sufficient for periodic layers with lossy materials due to abnormal field fluctuations between the layers. Thus, a more rigorous EMA with non-local corrections is needed to account for the variations introduced by plasmonic materials [121, 122]. Although I did not use such calculations here, it is important to understand the implications of non-local corrections in the design of HMMs and PHCs. Briefly, for low-order modes, plasmonic materials do not induce large variations in ε and can be approximated with the non-local corrections below. The need for these approximations decreases with increasing number of layers. Higher order modes in an HMM can be localized in areas as small as $\lambda/8$, reducing the accuracy of the non-local correction approximations, as these variations do not occur in all-dielectric or in larger scale periodic materials. The equations from Elser *et al.* are displayed below for completeness [122]:

$$\varepsilon_{xy}^{\text{eff}} = \frac{\varepsilon_{xy}^{(0)}}{1 - \delta_{xy}(k, \omega)}$$

$$\varepsilon_z^{\text{eff}} = \frac{\varepsilon_z^{(0)}}{1 - \delta_z(k, \omega)}$$

For the non-local corrections δ_{xy} and δ_z ($a_1 = f_1 p$, $a_2 = f_2 p$):

$$\delta_{xy} = \frac{a_1^2 a_2^2 (\varepsilon_1 - \varepsilon_2)^2 \omega^2}{12(a_1 + a_2)^2 \varepsilon_{xy}^{(0)} c^2}$$

$$\delta_z = \frac{a_1^2 a_2^2 (\varepsilon_1 - \varepsilon_2)^2 \varepsilon_z^{(0)2}}{12(a_1 + a_2)^2 \varepsilon_1^2 \varepsilon_2^2} \left(\varepsilon_{xy}^{(0)} \frac{\omega^2}{c^2} - \frac{k_x^2 (\varepsilon_1 + \varepsilon_2)^2}{\varepsilon_{xy}^{(0)}} \right)$$

where the choice of $k_x = 2\pi j/h$ instead of k_z or k_y for the j^{th} mode and $h = N_p p$ is somewhat arbitrary.

4.2.4 Fabrication Plan

The most difficult part of the fabrication process would be optimizing deposition in one chamber that can handle both Al and SiO₂, as removing the sample from vacuum between deposition layers will introduce oxidation of the Al layer. Previously published PHCs were fabricated by sputtering Ag and Al₂O₃ in the same chamber, with a thin seed layer of Ge before Ag to facilitate layer smoothness [111, 123]. Sputter deposition of Al introduces similar challenges without the addition of a thin metal (~ 1 nm to 2 nm) layer, such as Ti [124, 125]. Thus, the initial fabrication plan is to optimize sputter deposition of the materials to form thin layers in the repeating order SiO₂-Ti-Al.

After any deposition, it is important to note that the interface between Al and SiO₂ will not be pure due to the room-temperature reaction between the materials [126]. Once equilibrated to room temperature, it is thermodynamically favorable for O₂ at the interface to bind to Al instead of SiO₂, forming an Al-Al₂O₃-Si-SiO₂ structure. This effect does not occur in vacuum during the deposition process. However, the total thickness of this interface is no more than 1 nm to 2 nm, meaning that there is no need for an interface layer to mitigate negative effects of the oxidation-reduction reaction, as the interface layer would be just as thick [127, 128].

A wide variety of etchants and lithography tools are available to fabricate holes in the metamaterial structure [129]. Here, I propose focused ion beam milling as the final step in the PHC creation in order to etch holes on the surface [111]. While time consuming, it has an advantage over traditional etchants because of the multiple materials involved and because of the small feature sizes.

4.3 Results and Discussion

Here I show the polarization independent response of simulating (via S⁴ and FDTD) the PHC in Fig. 4.3c and Table 4.1, as described in the previous sections. This polarization independence is due to the hexagonal lattice symmetry of

the crystal. Using this PHC for biosensing, instead of the PC described in Chapter 3, means that increased laser power would be transmitted to the surface, not having been lost to the half wave plate or the polarizer. This allows the use of less complex optical setups and ensures that the laser has more than sufficient power. The PHC also does not require as stringent coupling conditions as the PC, so QD-conjugated biomarkers can be detected using a standard microscope.

4.3.1 PHC Response

The Cunningham group's current PCs require a cylindrical lens to focus light to a line, along with a method of adjusting the incident angle of the line on the surface. This is because a slight refractive index shift on the surface (due to the presence of the biomaterials) changes the coupling conditions, or the wavelength and angle at which maximum enhancement is achieved. Using the PHC, enhancement is slightly reduced in favor of increased bandwidth. This results in less stringent coupling conditions, yielding consistent enhancement at normal incidence that is relatively independent of refractive index shifts due to surface density changes or other biomaterial variations.

Figures 4.5a-b demonstrate the relatively broadband operation of the PHC. Reflected power is minimized at $\lambda = 450$ nm (Fig. 4.5a), while the θ response is unchanged for $\phi < 10^\circ$ (Fig. 4.5b). In Fig. 4.6a-b, both average and peak E_2 at the surface are maximized at $\lambda = 450$ nm, independent of polarization, as expected.

Cross-sections of the electromagnetic enhancement reveal what look analogous to modes (in traditional PCs) in the holes. At normal incidence (Fig. 4.7a/c), there is strong enhancement near the edges, with minimal enhancement in the center of the ridges. For QDs (or other reporters) sitting in or near the edges of the holes, $> 10\times$ average enhancement above the surface is predicted. This enhancement occurs for a wider band of angles than was possible with the previous generation of PCs. For off-angle response, the peak enhancement is slightly higher, but the field is not uniform and the average enhancement above the surface decreases as shown in Fig. 4.7b/d.

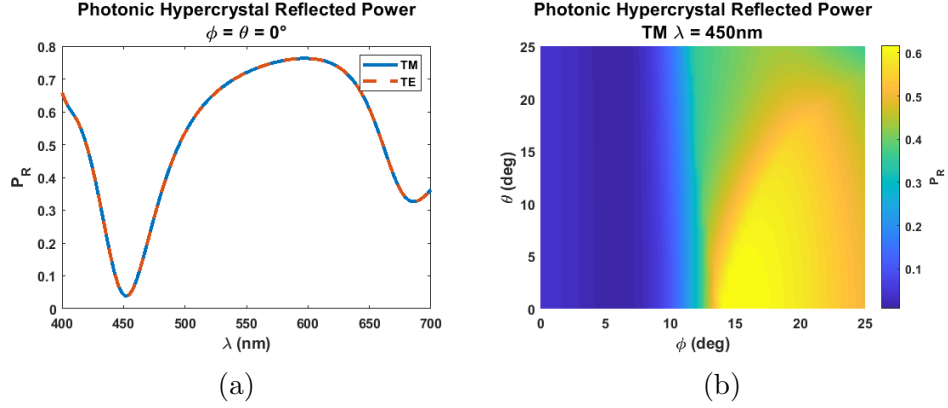


Fig. 4.5. Reflected power vs. (a) wavelength and (b) incident angle (ϕ/θ) for PHC.

4.3.2 Response of PC vs. PHC

As mentioned previously, PCs have a very large enhancement factor, but only for very stringent coupling conditions. The PHC has more uniform, although smaller, enhancement that is spread over a wider band of angles, reducing the need for custom equipment and specialized optics. This is demonstrated in Fig. 4.8a-b. Enhancements for the PC are $\sim 30\times$ larger than for the PHC, but the PHC yields enhancement over $100\times$ for $|\phi| < 10^\circ$ rather than the $\phi \approx 0.3^\circ$ range of the PC.

The wide bandwidth of the PHC is further exemplified in the band diagram of Fig. 4.9b. The stringent coupling conditions (shown by peak reflected power) of the PC are, again, in stark contrast to the wide band (shown by peak absorbed

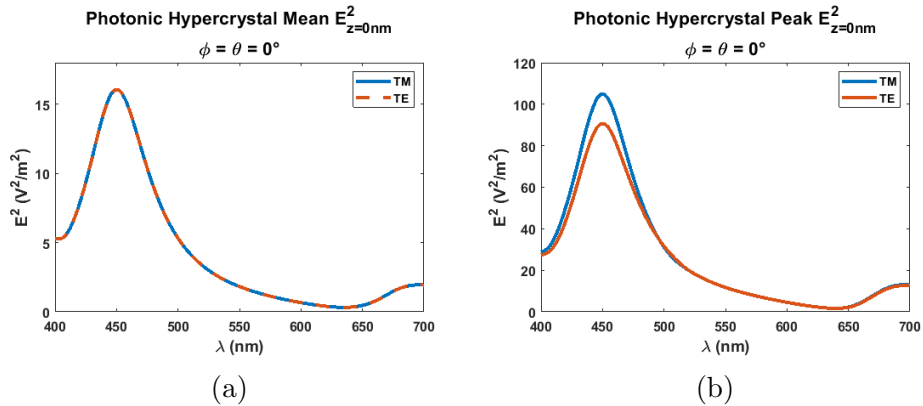


Fig. 4.6. (a) Average and (b) peak enhancement (at $z = 0$ nm) vs. wavelength for orthogonal polarizations.

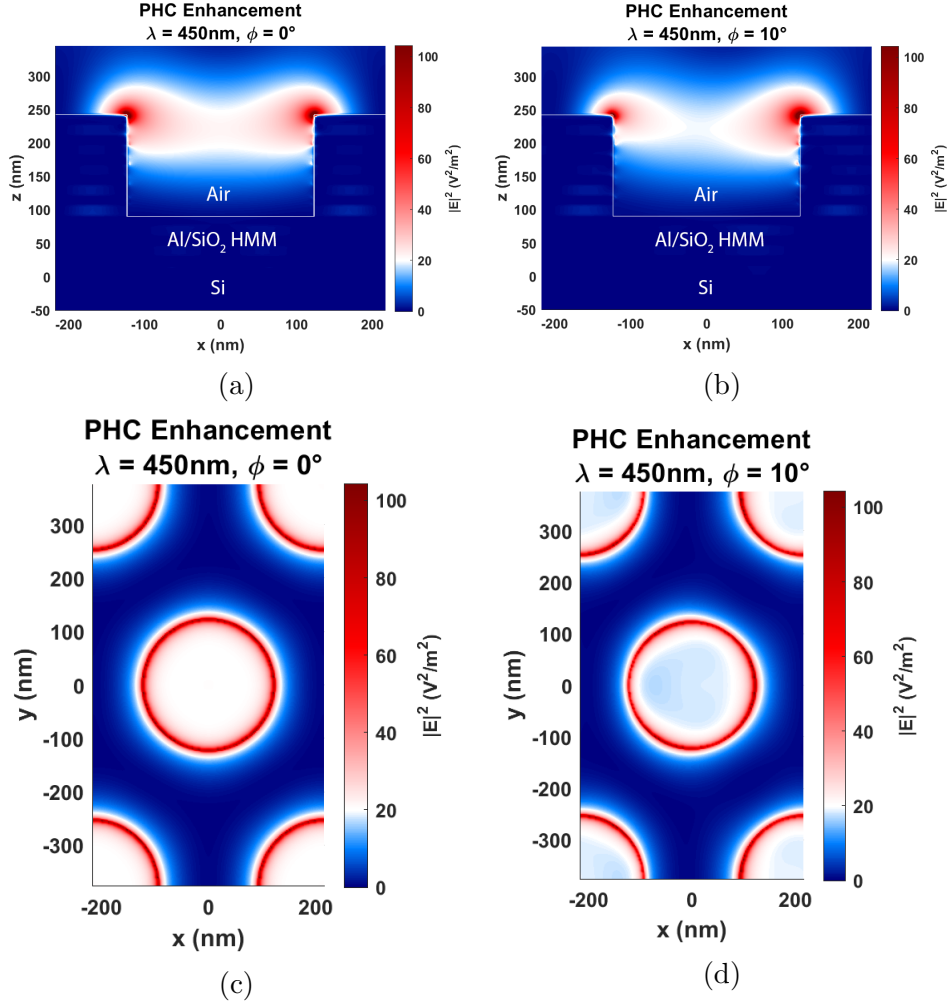


Fig. 4.7. Cross-sections of E^2 values in PHC for $\lambda = 450\text{ nm}$ and $\theta = 0^\circ$ at (a)/(c) maximum enhancement ($\phi = 0^\circ$) and (b)/(d) $\phi = 10^\circ$. (a) and (b) are at $y = 0$, while (c) and (d) are at $z = 0$ and represent the response of unpolarized light. High enhancement always occurs within and near the edges of the hole regions.

power) of the PHC. Any change in the refractive index on the PC surface will require an adjustment in angle to match the new coupling conditions, while the new coupling conditions remain within the band of high enhancement of the PHC.

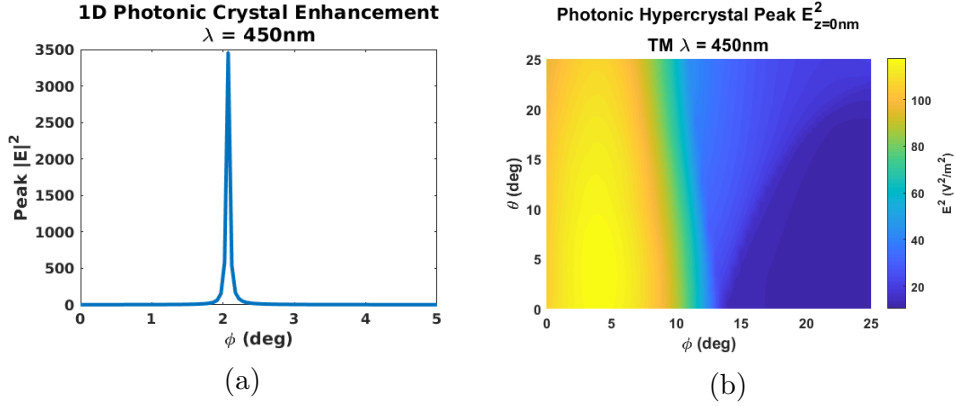


Fig. 4.8. Comparison of peak E^2 curves for a (a) PC resonant near $\lambda = 450$ nm and (b) a PHC designed to maximize enhancement at $\lambda = 450$ nm.

4.3.3 Biomarker Response

I have simulated (via FDTD) a biomarker as a sphere of radius $r = 50$ nm and RI $n = 1.5$. As shown in Fig. 4.10a-b, enhancement increases near the biomarker due to its interaction with the PHC. This means high enhancement at normal incidence is still achievable, even when materials with different refractive index are present on the PHC surface. For dielectric 1D photonic crystals, the presence of biomaterial on the surface requires angle tuning to achieve significant enhancement.

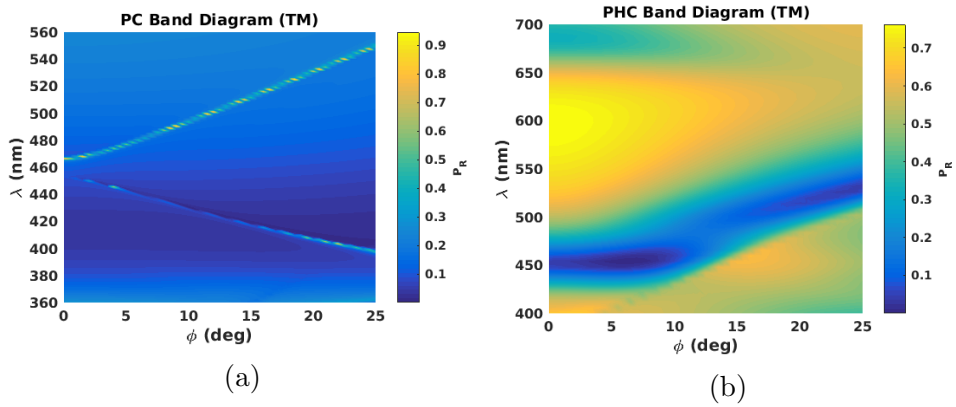


Fig. 4.9. Simulated band diagrams for (a) PC and (b) PHC. Yellow indicates high reflectivity, blue indicates low reflectivity. Note that enhancement is maximized in the PC at peak reflected power, and enhancement is maximized in the PHC at peak absorbed power. Symmetry holds for both cases that $P_R(\phi) = P_R(-\phi)$.

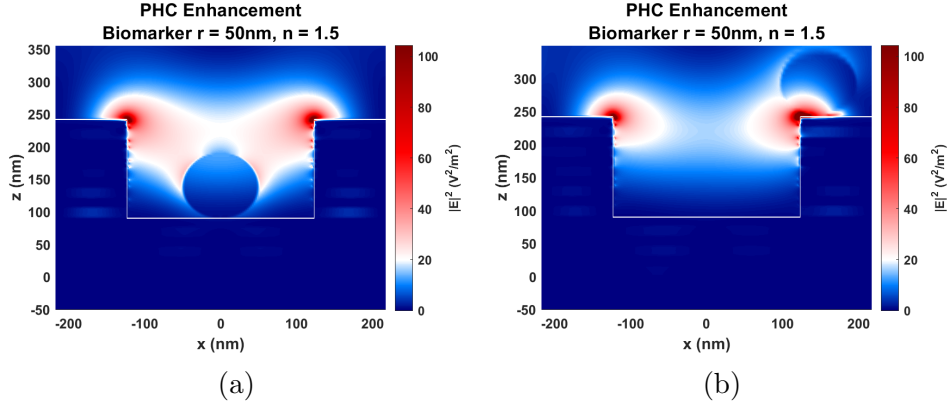


Fig. 4.10. Simulated PHC when $r = 50$ nm, $n = 1.5$ biomarker is located (a) in the hole and (b) on top of the ridge.

It is important to note that a uniform 50 nm layer of biomaterial on the PHC surface would not yield significant enhancement, but such is not the result of surface preparation. There would be a ~ 10 nm layer of silane, and actual bound biomarkers are not nearly as densely packed. If surface preparation significantly red-shifts the enhancement, it would be fairly simple to redesign the PHC with margin to account for the standard chemistries used. The 50 nm sphere was chosen to highlight the area in which a biomarker might be located to estimate the enhancement factor of a QD bound near the edge. This enhancement is significantly higher in the well ($> 20\times$) vs. outside of the well ($\sim 7\times$), as would be expected from the enhancement profiles in Fig. 4.7a. Given that the holes cover $\sim 30\%$ of the PHC surface area, this yields an average enhancement factor of $\sim 12\times$.

4.4 Conclusion and Future Work

I have designed and simulated a novel optical metamaterial configuration of a PHC that is capable of enhancing QD emission for biosensing applications. While a conventional PC has $> 30\times$ larger enhancement, a PHC facilitates enhancement over a much broader range of angles ($|\phi| < 10^\circ$). The PHC averages $\sim 15\times$ enhancement and peaks at $> 100\times$ enhancement at the surface. During the design process, I optimized and ascertained the physical effects of varying PHC parameters, leading to a repeatable process for producing future PHCs. Especially important for portable, low-cost healthcare applications is

the design of the PHC at $\lambda = 450$ nm where I believe its unique enhancement of QD-tagged biomarkers will have an especially meaningful impact. Future work will involve fabricating and characterizing this PHC followed by experimentally testing enhancement of QD-conjugated biomarkers.

CHAPTER 5

PHOTONIC CRYSTAL ENHANCED QUANTUM DOT EMISSION FOR MONITORING TREATMENT EFFICACY IN METASTATIC CASTRATE-RESISTANT PROSTATE CANCER

5.1 Introduction

5.1.1 Motivation

There exist a variety of treatment options for metastatic castrate-resistant prostate cancer (mCRPC), including targeted therapies [130–133], vaccines [134], chemotherapies [135], and other drugs. Given all of these options, with the prospect of many more [136], it is difficult to find the optimal drug therapy [130, 131]. Even tracking disease progression to determine whether a drug therapy is optimal is difficult for two main reasons: first, there are few uniform standards for evaluating patient progress; second, the therapy needs to be given enough time to be effective, as a tumor may initially grow before it begins to shrink [137, 138].

A new candidate for monitoring disease progression is androgen receptor variant (AR-V) expression in blood [139, 140]. The AR gene controls androgen signaling in prostate cells and consists of two main sections: an N-terminal domain and a variable domain. An AR-V differs from a full-length AR (AR-FL) in the variable domain. Certain AR-Vs have been shown to promote tumor progression and serve as biomarkers for monitoring therapies [141–144]. However, reliably detecting AR-Vs in blood has proven to be difficult, as

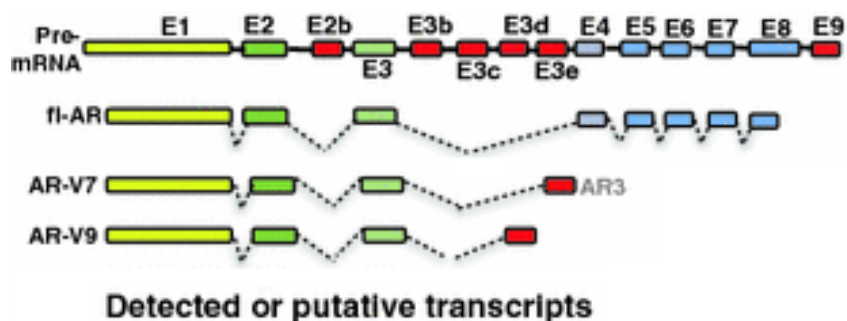
concentrations are in the attomolar (10^{-18} M) range, which requires single molecule sensitivity [145, 146].

In order to detect the AR-Vs, we propose using a modified version of fluorescence *in situ* hybridization (FISH) that is widely used to detect single-stranded DNA (ssDNA) and messenger RNA (mRNA) in tissue samples [147], as shown in Fig. 5.1a-b. Standard FISH has high enough sensitivity and specificity such that it can detect single molecules, with the technique being both reproducible and inexpensive. The three main steps to performing FISH are: first, fluorescently-tagged nucleic acid probes bind to complementary sequences of ssDNA or mRNA in sample; second, the signal is amplified with multiple fluorescently-tagged nucleic acid binding events; third, the sample is imaged using standard fluorescence microscopy. Traditional mRNA amplification (such as qRT-PCR) uses only a single nucleic acid binding event, but FISH uses 20-50 dyes on a strand with much higher sequence specificity and which emits a clearer signal, as shown in Fig. 5.2.

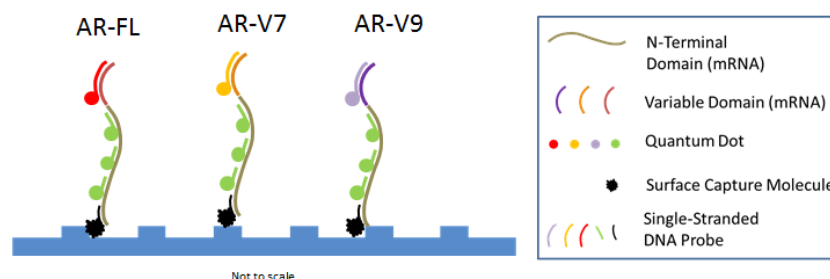
In order to quickly and reliably detect AR-Vs in blood, we will implement three improvements to FISH: first, our collaborators in the Smith group will tag mRNA with multiple colors using quantum dots (QDs) to detect both the AR-FLs and the AR-Vs, each with different sequences (Fig. 5.1b); second, we plan to use microfluidics to improve assay time and standardize work flow [79, 149]; finally, I plan to use a new photonic crystal (PC) and line-scanning detection instrument (both described in Chapter 3) for signal amplification and imaging. The ultimate goal is to have an automated, multiplexed method for the detection of single-molecules in blood. All that would be needed for the test is ~ 10 μ L of plasma, which is contained in just a few drops of blood from a finger-prick.

5.1.2 Significance

FISH is a proven, simple, low-cost mRNA sequence detection methodology that we plan to modify in order to detect AR-Vs, a biomarker for mCRPC, in a few droplets of blood. It is currently difficult to detect single molecules in blood using more traditional methods like qRT-PCR and mRNA sequencing, but FISH, typically used in tissue biopsy samples, will improve upon on that. The use of FISH will enable disease progression monitoring in mCRPC for



(a)



(b)

Fig. 5.1. (a) Depiction of N-terminal domain (yellow, E1) and variable domain (green, red, and blue) sequences for the AR-FL and AR-Vs. Adapted by permission from Springer Nature: [148], ©2011. (b) Modified FISH protocol utilizing QD tags for a liquid biopsy. The AR-V strands are held to the surface by capture probes, and multi-colored QDs are attached via ssDNA probes for imaging.

establishing the efficacy of a drug treatment regimen. Current methods for monitoring disease progression are yet not specific enough to be tailored to each patient's unique biology. Thus, we hope to improve outcomes and reduce treatment time for mCRPC patients.

5.1.3 Competing Approaches

Comparable DNA-based methods, including qRT-PCR, digital PCR (dPCR), and RNA sequencing, are either not sensitive enough or are too expensive. In particular, qRT-PCR only has femtomolar (10^{-15} M) sensitivity, 1000× less than what is needed for single-molecule detection [151]. dPCR is a relatively new technology. While being more precise than qRT-PCR, it has comparable sensitivity and requires more expensive equipment and more expertise [152, 153].

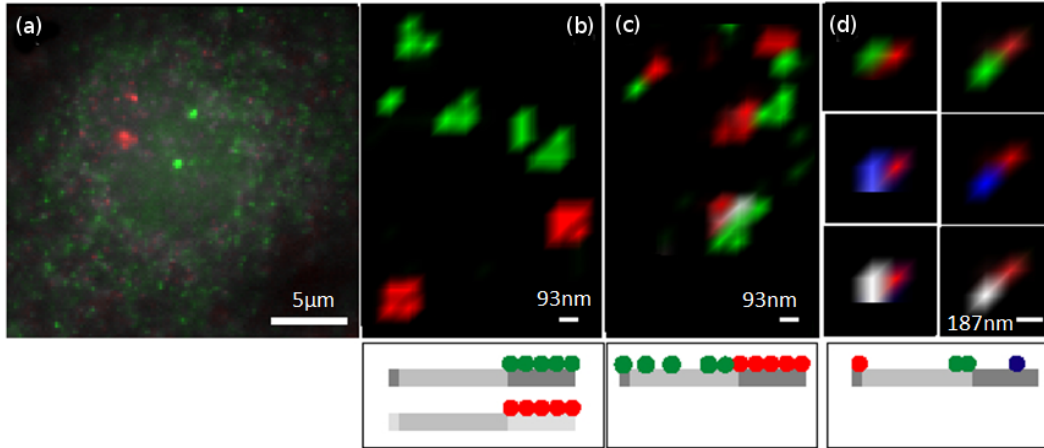


Fig. 5.2. (a) β - (green) γ - (red) actin mRNA in the cytoplasm of a cell. (b) Individual β - and γ -actin mRNA molecules. (c) The detection of *cis*-sequences in β -actin mRNA. (d) Intramolecular measurement in β -actin mRNA. Single-molecules are resolved with digital imaging and deconvolution techniques. From [150]. Reprinted with permission from AAAS.

Finally, RNA sequencing is still too expensive to justify repeated testing during drug therapy [137].

Different treatments produce different responses at different rates in different people, which makes the efficacy of any therapy nearly impossible to ascertain [137]. An example of this treatment/response unpredictability is the prostate-specific antigen (PSA) level. Even in an effective therapy, levels of PSA can rise before they begin to fall, making it a non-uniform indicator for treatment efficacy [137]. Another example of this unpredictability is imaging methods, including X-ray, CT scan, bone scan, and MRI, which can reveal mCRPC tumors in various organs and/or lymph nodes. These tumors not only take time to appear in scans, but they can also be too small to discern [137]. In bone scans, it is especially difficult to detect changes in bone metastasis size or intensity between scans, which are both indicators of mCRPC progression. Again, metastases in bone scans can appear to get larger before they shrink [137]. None of these options are reliable indicators on their own, and even combined, they can yield conflicting results without providing real-time insight into disease progression.

5.1.4 Innovation

In order more effectively perform the modified FISH assay, we plan to use a microfluidic system to both automate and expedite the assay process, to tag nucleic acid sequences in AR-Vs with multiple differently colored QDs, and to design custom PCs to amplify QD output for single-molecule detection. These three steps will enable a reduction in the amount of time and equipment needed for performing the assay, enabling point-of-care detection. This unique combination of chemistry, microfluidics, and engineering will allow the reliable, inexpensive detection outside of the traditional lab environment.

PCs for enhancing multicolor QD-tagged ARs

The Cunningham group has previously designed PCs to enhance QD emission [100–103]. However, these all reported enhanced QD output at a single emission wavelength. The Cunningham group has also previously shown that enhancing QD excitation alone will enhance the emission [103], but this is, to our knowledge, the first effort to use one PC surface to enhance the output of multiple colors of QDs.

QDs have previously been used in FISH [154, 155], but nobody to our knowledge has amplified either QD or fluorescent dye emission to make the method more sensitive. FISH already has single-molecule sensitivity, so the goal is that QD-coupled PCs will increase the visibility and robustness of the assay.

Spectroscopic line scanner and analysis

As the line scanner is unique to the enhancement of the Cunningham group PCs, any improvements made it are novel. The innovation here is the combination of custom hardware and software with the goal of automated assay analysis, from performing the PC surface scans to analyzing the resulting spectra and reporting a count of AR-Vs. We are working toward the development of an all-in-one platform for detection and analysis of biomarkers for disease screening and progression monitoring.

5.2 Methods

I have designed a PC resonant near $\lambda = 450$ nm and built a line scanning instrument to enhance and detect the QD output as described in Chapter 3. Briefly, QDs are semiconductor nanoparticles that can be tuned to emit visible light at intensity up to $1000\times$ that of fluorescent dyes [156]. They can be attached to nucleic acids that bind with mRNA for FISH [157], and their resistance to photobleaching, broad excitation spectra, and high quantum-yield make them ideal for generating stable, robust signals [92]. The PCs are designed to enhance excitation of the QDs, as the emission wavelengths in the visible regime range from 525 nm to 685 nm. Enhanced excitation should also increase the emission of the QDs while facilitating the performance of FISH assays with multiplexed detection of AR-Vs [103].

5.2.1 PCEF System Validation

The design and fabrication of these PCs was thoroughly described in Chapter 3. Briefly, I have designed a new PC for excitation with a 450 nm laser to overlap with QD excitation. It is fabricated with a 28.1 nm SiO_2 grating ($\Lambda = 295$ nm, $f_c = 38.5\%$) on a fused silica substrate. This is overcoated with a 112 nm thick Si_3N_4 layer. Each wafer is then diced into $12\text{ mm} \times 25\text{ mm}$ pieces for performing assays.

Around 100 nm above the surface, the PC has an ideal enhancement factor of $\sim 50\times$. Accounting for variations during fabrication, I expect an enhancement factor of $\sim 10 - 15\times$. Based on experimental work, I expect a resonance angle shift of 5° to 8° to couple the 450 nm laser to the surface functionalized with QD-tagged AR-Vs.

Given that preliminary validation of QD enhancement was completed in Chapter 3, the task here will be to validate enhancement of QD-tagged AR-Vs on a PC surface. However, supplies of patient AR-Vs are limited, so we plan to do this with commercially available, custom mRNA sequences. The first step is to work with our collaborators to get the surface chemistry correct such that mRNA are immobilized and dried on the PC surface. Current members of the Cunningham lab have performed this successfully and are working to adapt the technique for this project. One area we are actively exploring is how to dry the biomarkers on the PC surface, given that imaging them in solution is

non-ideal with the low-NA lens in the current PCEF setup. Future integration with the microfluidic chip will eliminate this issue (see Chapter 2).

The second step is to validate enhancement of QDs with varying emission wavelengths. This will first be performed with mRNAs that are only tagged with one QD type at a time. Once we measure enhancement factor profiles and emission intensities for all QDs separately, then we can start investigating performance of the PC with multicolored QDs.

Finally, both the scanning and analysis software were improved significantly for speed and ease of use in Chapter 2. Preliminary validation of line scanner results and images was performed as a part of the work in Chapter 3. However, once we get multicolored mRNAs, we need to validate the spectral results against known locations and transcription sequences (via color) of the mRNAs. Spectral line scanning is already functional (Fig. 5.3a-c), but we need to optimize the EMCCD camera settings after finalizing the assay protocol. Then, we will validate location finding and color calibration with known mRNA samples in an assay on the PC surface. This will be done in conjunction with validation of the QD enhancement as described previously.

5.2.2 Spectral Image Collection and Analysis

The redesign of the line scanning detection system was also thoroughly described in Chapter 3. Briefly, the Cunningham group has the capability to use both red ($\lambda = 637$ nm) and blue ($\lambda = 450$ nm) laser light for excitation of fluorescent dyes or QDs. The PCEF system is a customized microscope that focuses light to a line, rather than a point, on the functionalized surface to couple light into the PC using one precise angle. This line is then focused on the entrance slit of a Czerny-Turner spectrophotometer, which can be in either spectral or imaging mode depending on whether the turret is rotated to a $300 \ell/\text{mm}$ grating or a mirror.

I propose using the line scanner in spectrometer mode to obtain the spectrum of each location on the PC. This will require custom software to analyze this spectral data to both map multiplexed QD emissions to their respective regions on the PC and to match these to corresponding mRNAs (and, later, AR-Vs). In other words, we need to generate a map of the AR-V locations using spectral

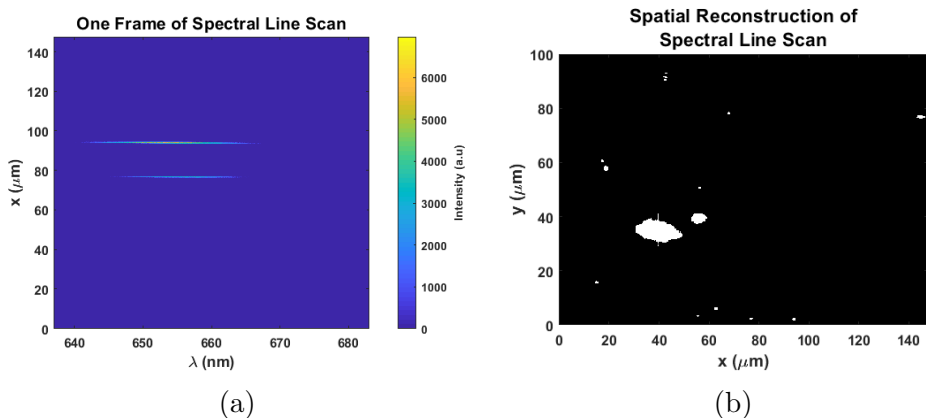


Fig. 5.3. Spatial reconstruction of spectral line scans. (a) Single frame of spectral line scan ($y \approx 2.6 \mu\text{m}$), where the x -axis is the spectral direction and the y -axis is the laser line. Two QDs can be seen by their spectral center $\sim 655 \text{ nm}$. (b) By collapsing all QD spectra found in (a) into one dimension, each line is stacked to form the spatial image. (c) Fluorescence scan for comparison to spectral reconstruction of (b). Bright spots are aggregate artifacts.

data. The aggregate data should then enable the reporting of a count of each type of detected AR-V for interpretation by an oncologist.

5.3 Conclusion and Future Work

In this chapter, I have proposed a new method of monitoring treatment for mCRPC, taking advantage of PC and QD technology that exists at the University of Illinois. We plan to use PCs and QDs to multiplex and amplify detection of AR-Vs, a biomarker for mCRPC, at the single-molecule sensitivity level. The goal is to make this a low-cost, portable instrument for point-of-care detection that can be expanded to other diseases with different biomarkers.

Much of the work here is built off previous papers and has been preliminarily completed as described in Chapter 3. The main objective is to integrate enhancement of multiplexed QDs conjugated to mRNA and, eventually, AR-Vs

using the newly designed PC and upgraded line scanner. We are currently in the process of exploring the assay protocol to achieve dried QD-conjugated ssDNA bound to the PC surface. This improves resolution and collection efficiency because light from the QDs cannot scatter in solution or through the PC while traveling to the objective.

The largest complication I anticipate is the potential for variable amplification of the QDs bound to the AR-Vs. Previous work has only used amplification of one layer of fluorophores ~ 200 nm above the PC surface. In this proposal, there will be QDs extending the length of the AR-V from ~ 50 nm to a few hundred nanometers, depending on the conformation of the DNA. There is significant enhancement at 50 nm but no enhancement beyond ~ 200 nm. This could present a complication both when trying to count QDs, as they will not be of uniform intensity, and when trying to enhance emission of the QDs. I plan to fully characterize enhancement in the vertical direction and potentially explore options for projecting the AR-Vs parallel to the PC surface if sensitivity remains low.

CHAPTER 6

CONCLUSIONS

In this work, I have described a photonic crystal and line scanning detection/analysis system to aid in the screening and treatment monitoring of two types of cancer: oropharyngeal cancer (OPC) and metastatic castrate-resistant prostate cancer (mCRPC). I first developed an automated protocol for instrumentation used to improve screening for OPC, which can also be used for future disease biomarkers. I also detailed the design and testing of a new system that will be used to image quantum dot-tagged messenger RNA variants as a disease progression marker for mCRPC. Finally, I introduced a design using hyperbolic metamaterials in photonic crystals, forming photonic hypercrystals, to improve control over light-matter interaction.

All of these developments progress toward the ultimate goal of a portable, low-cost detection system to advance the screening for and tracking of diseases, including, but not limited to, cancer. More specifically, I have improved automation of the spot detection and data analysis, reducing error-prone manual work and decreasing the time to results. I also improved the utility of the detection system by facilitating the use of quantum dots instead of fluorophores, improving brightness and decreasing photobleaching for applications requiring high sensitivity. Finally, by exploring metamaterials, I expanded the utility of photonic hypercrystals for biosensing. These new materials offer unusual physics not possible in dielectrics and provide the flexibility for further design customizations and device improvements.

All of these technologies will improve future work on photonic crystal enhanced fluorescence (and quantum dots) by both expanding disease screening capabilities and simplifying optical detection setups. They will also allow the next generation of researchers to use advances in inexpensive CMOS cameras and 3D printing technology to make affordable screening devices available outside of traditional lab settings, making healthcare more accessible.

REFERENCES

- [1] “Cancer — early diagnosis and screening,” 2017. [Online]. Available: <http://www.who.int/cancer/prevention/diagnosis-screening/en/>
- [2] “Cancer screening guidelines — detecting cancer early,” 2017. [Online]. Available: <https://www.cancer.org/healthy/find-cancer-early/cancer-screening-guidelines/american-cancer-society-guidelines-for-the-early-detection-of-cancer.html>
- [3] B. W. Stewart and C. P. Wild, “World cancer report 2014,” *World Health Organization*, pp. 15–630, 2014.
- [4] J. Wilson and G. Jungner, “Principles and practice of screening for disease,” *Geneva: WHO*, no. 34, 1968.
- [5] H. J. de Koning, *The mysterious mass(es) [Inaugural address, Professor of Screening Evaluation]*. Rotterdam, The Netherlands: Erasmus MC, 2009.
- [6] H. Inan *et al.*, “Photonic crystals: Emerging biosensors and their promise for point-of-care applications,” *Chemical Society Reviews*, vol. 46, no. 2, pp. 366–388, Jan. 2017.
- [7] S. George *et al.*, “Sensitive detection of protein and miRNA cancer biomarkers using silicon-based photonic crystals and a resonance coupling laser scanning platform,” *Lab on a Chip*, vol. 13, no. 20, pp. 4053–64, 2013.
- [8] A. C. Wong, D. W. Wright, and J. A. Conrad, “Functionalized gold nanoparticles for detection of cancer biomarkers,” in *General Methods in Biomarker Research and their Applications*, V. R. Preedy and V. B. Patel, Eds. Springer, Netherlands, 2015, vol. 2-2, pp. 1143–1175.
- [9] X. Qian *et al.*, “*In vivo* tumor targeting and spectroscopic detection with surface-enhanced Raman nanoparticle tags,” *Nature Biotechnology*, vol. 26, no. 1, pp. 83–90, Dec. 2007.
- [10] B. T. Cunningham, M. Zhang, Y. Zhuo, L. E. Kwon, and C. M. Race, “Recent advances in biosensing with photonic crystal surfaces: A review,” *IEEE Sensors Journal*, vol. 16, no. 10, pp. 3349–3366, May 2016.
- [11] M. R. Foreman, J. D. Swaim, and F. Vollmer, “Whispering gallery mode sensors,” *Advances in Optics and Photonics*, vol. 7, no. 2, p. 168, June 2015.

- [12] S. T. Peng, T. Tamir, and H. L. Bertoni, "Theory of periodic dielectric waveguides," *IEEE Transactions on Microwave Theory and Techniques*, vol. 23, no. 1, pp. 123–133, Jan. 1975.
- [13] S. Tibuleac and R. Magnusson, "Reflection and transmission guided-mode resonance filters," *Journal of the Optical Society of America A*, vol. 14, no. 7, p. 1617, July 1997.
- [14] S. S. Wang and R. Magnusson, "Theory and applications of guided-mode resonance filters," *Applied Optics*, vol. 32, no. 14, pp. 2606–2613, May 1993.
- [15] J. M. Elson, L. F. DeSandre, and J. L. Stanford, "Analysis of anomalous resonance effects in multilayer-overcoated, low-efficiency gratings," *J. Opt. Soc. Am. A*, vol. 5, no. 1, pp. 74–88, Jan. 1988.
- [16] S. M. Norton, "Resonant grating structures: Theory, design, and applications," doctoral dissertation, The University of Rochester, 1998.
- [17] J.-N. Liu, M. V. Schulmerich, R. Bhargava, and B. T. Cunningham, "Sculpting narrowband Fano resonances inherent in the large-area mid-infrared photonic crystal microresonators for spectroscopic imaging," *Optics Express*, vol. 22, no. 15, pp. 18 142–58, July 2014.
- [18] V. M. Passaro, B. Troia, M. L. Notte, and F. D. Leonardis, "Photonic resonant microcavities for chemical and biochemical sensing," *RSC Advances*, vol. 3, no. 1, pp. 25–44, Nov. 2013.
- [19] L. Babić and M. J. A. de Dood, "Interpretation of Fano lineshape reversal in the reflectivity spectra of photonic crystal slabs," *Optics Express*, vol. 18, no. 25, pp. 26 569–82, Dec. 2010.
- [20] J. D. Joannopoulos, S. Johnson, J. N. Winn, and R. D. Meade, *Photonic Crystals: Molding the Flow of Light*, 2nd ed. Princeton University Press, 2008.
- [21] S. Fan and J. D. Joannopoulos, "Analysis of guided resonances in photonic crystal slabs," *Physical Review B*, vol. 65, no. 23, p. 235112, June 2002.
- [22] E. Yablonovitch and T. J. Gmitter, "Photonic band structure: The face-centered-cubic case," *Physical Review Letters*, vol. 63, no. 18, pp. 1950–1953, Oct. 1989.
- [23] X. Fan *et al.*, "Sensitive optical biosensors for unlabeled targets: A review," *Analytica Chimica Acta*, vol. 620, no. 1-2, pp. 8–26, July 2008.
- [24] S. M. Borisov and O. S. Wolfbeis, "Optical biosensors," *Chemical Reviews*, vol. 108, no. 2, pp. 423–461, 2008.

- [25] M. A. Cooper, “Optical biosensors in drug discovery,” *Nature Reviews Drug Discovery*, vol. 1, no. 7, pp. 515–528, July 2002.
- [26] B. Chocarro-Ruiz, A. Fernández-Gavela, S. Herranz, and L. M. Lechuga, “Nanophotonic label-free biosensors for environmental monitoring,” *Current Opinion in Biotechnology*, vol. 45, pp. 175–183, June 2017.
- [27] C. R. Taitt, G. P. Anderson, and F. S. Ligler, “Evanescent wave fluorescence biosensors: Advances of the last decade,” *Biosensors and Bioelectronics*, vol. 76, pp. 103–112, Feb. 2016.
- [28] K. Misiakos *et al.*, “All-silicon monolithic Mach-Zehnder interferometer as a refractive index and bio-chemical sensor,” *Optics Express*, vol. 22, no. 22, p. 26803, Nov. 2014.
- [29] E. Benito-Peña, M. G. Valdés, B. Glahn-Martínez, and M. C. Moreno-Bondi, “Fluorescence based fiber optic and planar waveguide biosensors. A review,” *Analytica Chimica Acta*, vol. 943, pp. 17–40, Nov. 2016.
- [30] C. A. Barrios *et al.*, “Label-free optical biosensing with slot-waveguides,” *Optics Letters*, vol. 33, no. 7, pp. 708–710, Apr. 2008.
- [31] F. Prieto *et al.*, “An integrated optical interferometric nanodevice based on silicon technology for biosensor applications,” *Nanotechnology*, vol. 14, no. 8, pp. 907–912, Aug. 2003.
- [32] N. Kinrot and M. Nathan, “Investigation of a periodically segmented waveguide Fabry-Perot interferometer for use as a chemical/biosensor,” *Journal of Lightwave Technology*, vol. 24, no. 5, pp. 2139–2145, May 2006.
- [33] Q. Liu, J. S. Kee, and M. K. Park, “A refractive index sensor design based on grating-assisted coupling between a strip waveguide and a slot waveguide,” *Optics Express*, vol. 21, no. 5, pp. 5897–909, Mar. 2013.
- [34] S. L. Chuang, *Physics of Photonic Devices*. John Wiley & Sons, 2009.
- [35] M. J. Levene *et al.*, “Zero-mode waveguides for single-molecule analysis at high concentrations,” *Science*, vol. 299, no. 5607, pp. 682–6, Jan. 2003.
- [36] F. Vollmer *et al.*, “Protein detection by optical shift of a resonant microcavity,” *Applied Physics Letters*, vol. 80, no. 21, pp. 4057–4059, May 2002.
- [37] F. Vollmer and S. Arnold, “Whispering-gallery-mode biosensing: label-free detection down to single molecules,” *Nature Methods*, vol. 5, no. 7, pp. 591–596, July 2008.

- [38] S. I. Shopova, R. Rajmangal, S. Holler, and S. Arnold, “Plasmonic enhancement of a whispering-gallery-mode biosensor for single nanoparticle detection,” *Applied Physics Letters*, vol. 98, no. 24, p. 243104, June 2011.
- [39] J. N. Anker *et al.*, “Biosensing with plasmonic nanosensors,” *Nature Materials*, vol. 7, no. 6, pp. 442–453, June 2008.
- [40] K. A. Willets and R. P. Van Duyne, “Localized surface plasmon resonance spectroscopy and sensing,” *Annual Review of Physical Chemistry*, vol. 58, no. 1, pp. 267–297, May 2007.
- [41] B. Špačková, P. Wrobel, M. Bocková, and J. Homola, “Optical biosensors based on plasmonic nanostructures: A review,” *Proceedings of the IEEE*, vol. 104, no. 12, pp. 2380–2408, Dec. 2016.
- [42] P. Englebienne, “Use of colloidal gold surface plasmon resonance peak shift to infer affinity constants from the interactions between protein antigens and antibodies specific for single or multiple epitopes,” *The Analyst*, vol. 123, no. 7, pp. 1599–1603, Jan. 1998.
- [43] A. V. Kabashin *et al.*, “Plasmonic nanorod metamaterials for biosensing,” *Nature Materials*, vol. 8, no. 11, pp. 867–871, Nov. 2009.
- [44] M. C. Estevez, M. A. Otte, B. Sepulveda, and L. M. Lechuga, “Trends and challenges of refractometric nanoplasmonic biosensors: A review,” *Analytica Chimica Acta*, vol. 806, pp. 55–73, Jan. 2014.
- [45] A. J. Haes, L. Chang, W. L. Klein, and R. P. Van Duyne, “Detection of a biomarker for Alzheimer’s disease from synthetic and clinical samples using a nanoscale optical biosensor,” *Journal of the American Chemical Society*, vol. 127, no. 7, pp. 2264–2271, 2005.
- [46] A. Ameen *et al.*, “Plasmonic sensing of oncoproteins without resonance shift using 3D periodic nanocavity in nanocup arrays,” *Advanced Optical Materials*, vol. 5, no. 11, p. 1601051, June 2017.
- [47] O. Limaj *et al.*, “Infrared plasmonic biosensor for real-time and label-free monitoring of lipid membranes,” *Nano Letters*, vol. 16, no. 2, pp. 1502–1508, Feb. 2016.
- [48] R. Regmi *et al.*, “All-dielectric silicon nanogap antennas to enhance the fluorescence of single molecules,” *Nano Letters*, vol. 16, no. 8, pp. 5143–5151, Aug. 2016.
- [49] M. Caldarola *et al.*, “Non-plasmonic nanoantennas for surface enhanced spectroscopies with ultra-low heat conversion,” *Nature Communications*, vol. 6, p. 7915, Aug. 2015.

- [50] J. Cambiasso *et al.*, “Bridging the gap between dielectric nanophotonics and the visible regime with effectively lossless gallium phosphide antennas,” *Nano Letters*, vol. 17, no. 2, pp. 1219–1225, Feb. 2017.
- [51] C. V. Raman, “A new radiation,” *Indian Journal of Physics*, vol. 2, pp. 387–398, 1928.
- [52] E. Petryayeva and U. J. Krull, “Localized surface plasmon resonance: Nanostructures, bioassays and biosensing - A review,” *Analytica Chimica Acta*, vol. 706, no. 1, pp. 8–24, Nov. 2011.
- [53] D. L. Jeanmaire and R. P. Van Duyne, “Surface Raman spectroelectrochemistry,” *Journal of Electroanalytical Chemistry and Interfacial Electrochemistry*, vol. 84, no. 1, pp. 1–20, Nov. 1977.
- [54] X. Fu *et al.*, “A SERS-based lateral flow assay biosensor for highly sensitive detection of HIV-1 DNA,” *Biosensors and Bioelectronics*, vol. 78, pp. 530–537, Apr. 2016.
- [55] X. Wang *et al.*, “Simultaneous detection of dual nucleic acids using a SERS-based lateral flow assay biosensor,” *Analytical Chemistry*, vol. 89, no. 2, pp. 1163–1169, Jan. 2017.
- [56] C. Fu *et al.*, “Surface-enhanced Raman scattering (SERS) biosensing based on nanoporous dielectric waveguide resonance,” *Sensors and Actuators, B: Chemical*, vol. 201, pp. 173–176, Oct. 2014.
- [57] P. Zheng *et al.*, “A gold nanohole array based surface-enhanced Raman scattering biosensor for detection of silver(i) and mercury(ii) in human saliva,” *Nanoscale*, vol. 7, no. 25, pp. 11 005–11 012, June 2015.
- [58] O. Yavas, M. Svedendahl, P. Dobosz, V. Sanz, and R. Quidant, “On-chip biosensing based on all-dielectric nanoresonators,” *Nano Letters*, vol. 17, no. 7, pp. 4421–4426, July 2017.
- [59] N. Bontempi *et al.*, “Highly sensitive biosensors based on all-dielectric nanoresonators,” *Nanoscale*, vol. 9, no. 15, pp. 4972–4980, Apr. 2017.
- [60] J. B. Pendry, A. J. Holden, D. J. Robbins, and W. J. Stewart, “Magnetism from conductors and enhanced nonlinear phenomena,” *IEEE Transactions on Microwave Theory and Techniques*, vol. 47, no. 11, pp. 2075–2084, 1999.
- [61] D. R. Smith, J. B. Pendry, and M. C. K. Wiltshire, “Metamaterials and negative refractive index,” *Science*, vol. 305, no. 5685, pp. 788–792, 2004.
- [62] V. G. Veselago, “The electrodynamics of substances with simultaneously negative values of ϵ and μ ,” *Soviet Physics Uspekhi*, vol. 10, no. 4, pp. 509–514, Apr. 1968.

- [63] J. B. Pendry, “Negative refraction makes a perfect lens,” *Physical Review Letters*, vol. 85, no. 18, pp. 3966–3969, Oct. 2000.
- [64] D. Schurig *et al.*, “Metamaterial electromagnetic cloak at microwave frequencies,” *Science*, vol. 314, no. 5801, pp. 977–980, 2006.
- [65] F. Aieta *et al.*, “Aberration-free ultrathin flat lenses and axicons at telecom wavelengths based on plasmonic metasurfaces,” *Nano letters*, vol. 12, no. 9, pp. 4932–6, Sep. 2012.
- [66] E. E. Narimanov, “Photonic hypercrystals,” *Physical Review X*, vol. 4, no. 4, p. 041014, Oct. 2014.
- [67] M. I. D’yakonov, “New type of electromagnetic wave propagating at an interface,” *Sov Phys JETP*, vol. 67, no. April, pp. 714–716, 1988.
- [68] F. Abbas, A. Lakhtakia, Q. A. Naqvi, and M. Faryad, “An optical-sensing modality that exploits Dyakonov-Tamm waves,” *Photonics Research*, vol. 3, no. 1, p. 5, Feb. 2015.
- [69] W. Zhu, T. Xu, A. Agrawal, and H. J. Lezec, “High-contrast nanoparticle sensing using a hyperbolic metamaterial,” *CLEO: 2015*, vol. 1, p. FF2C.1, May 2015.
- [70] V. G. Kravets *et al.*, “Singular phase nano-optics in plasmonic metamaterials for label-free single-molecule detection,” *Nature Materials*, vol. 12, no. 4, pp. 304–309, Apr. 2013.
- [71] K. V. Sreekanth *et al.*, “Extreme sensitivity biosensing platform based on hyperbolic metamaterials,” *Nature Materials*, vol. 15, no. 6, pp. 621–627, Mar. 2016.
- [72] N. Vasilantonakis, G. A. Wurtz, V. A. Podolskiy, and A. V. Zayats, “Refractive index sensing with hyperbolic metamaterials: Strategies for biosensing and nonlinearity enhancement,” *Optics Express*, vol. 23, no. 11, p. 14329, June 2015.
- [73] C. A. Moody and L. A. Laimins, “Human papillomavirus oncoproteins: pathways to transformation,” *Nature Reviews Cancer*, vol. 10, no. 8, pp. 550–560, Aug. 2010.
- [74] S. Marur, G. D’Souza, W. H. Westra, and A. A. Forastiere, “HPV-associated head and neck cancer: A virus-related cancer epidemic,” *The Lancet Oncology*, vol. 11, no. 8, pp. 781–789, Aug. 2010.
- [75] G. D’Souza *et al.*, “Oral human papillomavirus (HPV) infection in HPV-positive patients with oropharyngeal cancer and their partners,” *Journal of Clinical Oncology*, vol. 32, no. 23, pp. 2408–2415, Aug. 2014.

- [76] G. D'Souza *et al.*, "Case-control study of human papillomavirus and oropharyngeal cancer," *New England Journal of Medicine*, vol. 356, no. 19, pp. 1944–1956, May 2007.
- [77] K. S. Anderson *et al.*, "Serum antibodies to the HPV16 proteome as biomarkers for head and neck cancer," *British Journal of Cancer*, vol. 104, no. 12, pp. 1896–1905, June 2011.
- [78] C. M. Race *et al.*, "An automated microfluidic assay for photonic crystal enhanced detection and analysis of an antiviral antibody cancer biomarker in serum," *IEEE Sensors Journal*, vol. 18, no. 4, pp. 1464–1473, Feb. 2018.
- [79] Y. Tan, T. Tang, H. Xu, C. Zhu, and B. T. Cunningham, "High sensitivity automated multiplexed immunoassays using photonic crystal enhanced fluorescence microfluidic system," *Biosensors and Bioelectronics*, vol. 73, pp. 32–40, 2015.
- [80] V. Chaudhery *et al.*, "Line-scanning detection instrument for photonic crystal enhanced fluorescence," *Optics Letters*, vol. 37, no. 13, p. 2565, July 2012.
- [81] S. I. Jones *et al.*, "Direct detection of transcription factors in cotyledons during seedling development using sensitive silicon-substrate photonic crystal protein arrays," *Plant Physiology*, vol. 167, no. 3, 2015.
- [82] Y. Tan *et al.*, "Application of photonic crystal enhanced fluorescence to detection of low serum concentrations of human IgE antibodies specific for a purified cat allergen (Fel D1)," *Biosensors and Bioelectronics*, vol. 77, pp. 194–201, 2016.
- [83] J. Bernsen, "Dynamic thresholding of grey-level images," in *Proceedings - International Conference on Pattern Recognition*. IEEE, 1986, pp. 1251–1255.
- [84] A. M. White, D. S. Daly, and R. C. Zangar, "Analysis of high-throughput ELISA microarray data," in *Bioinformatics for Comparative Proteomics: Methods in Molecular Biology*. Humana Press, 2011, vol. 694, pp. 191–211.
- [85] A. M. Smith, H. Duan, A. M. Mohs, and S. Nie, "Bioconjugated quantum dots for *in vivo* molecular and cellular imaging," *Advanced Drug Delivery Reviews*, vol. 60, no. 11, pp. 1226–1240, Aug. 2008.
- [86] S. J. Lim *et al.*, "Brightness-equalized quantum dots," *Nature Communications*, vol. 6, p. 8210, Oct. 2015.

- [87] X. Wu *et al.*, “Immunofluorescent labeling of cancer marker HER2 and other cellular targets with semiconductor quantum dots,” *Nature Biotechnology*, vol. 21, no. 1, pp. 41–46, Dec. 2002.
- [88] A. M. White *et al.*, “ProMAT: Protein microarray analysis tool,” *Bioinformatics*, vol. 22, no. 10, pp. 1278–1279, May 2006.
- [89] H. Inan *et al.*, “Isolation, detection, and quantification of cancer biomarkers in HPV-associated malignancies,” *Scientific Reports*, vol. 7, no. 1, p. 3322, Dec. 2017.
- [90] J. K. Jaiswal, H. Mattoussi, J. M. Mauro, and S. M. Simon, “Long-term multiple color imaging of live cells using quantum dot bioconjugates,” *Nature Biotechnology*, vol. 21, no. 1, pp. 47–51, Dec. 2003.
- [91] D. S. Lidke *et al.*, “Quantum dot ligands provide new insights into erbB/HER receptor-mediated signal transduction,” *Nature Biotechnology*, vol. 22, no. 2, pp. 198–203, Feb. 2004.
- [92] I. L. Medintz, H. T. Uyeda, E. R. Goldman, and H. Mattoussi, “Quantum dot bioconjugates for imaging, labelling and sensing,” *Nature Materials*, vol. 4, no. 6, pp. 435–446, June 2005.
- [93] M. Han, X. Gao, J. Z. Su, and S. Nie, “Quantum-dot-tagged microbeads for multiplexed optical coding of biomolecules,” *Nature Biotechnology*, vol. 19, no. 7, pp. 631–635, July 2001.
- [94] J. V. Jokerst *et al.*, “Nano-bio-chips for high performance multiplexed protein detection: Determinations of cancer biomarkers in serum and saliva using quantum dot bioconjugate labels,” *Biosensors and Bioelectronics*, vol. 24, no. 12, pp. 3622–3629, Aug. 2009.
- [95] M. Hu *et al.*, “Ultrasensitive, multiplexed detection of cancer biomarkers directly in serum by using a quantum dot-based microfluidic protein chip,” *ACS Nano*, vol. 4, no. 1, pp. 488–494, Jan. 2010.
- [96] W. C. Chan and S. Nie, “Quantum dot bioconjugates for ultrasensitive nonisotopic detection,” *Science*, vol. 281, no. 5385, pp. 2016–2018, 1998.
- [97] X. Gao, Y. Cui, R. M. Levenson, L. W. K. Chung, and S. Nie, “*In vivo* cancer targeting and imaging with semiconductor quantum dots,” *Nature Biotechnology*, vol. 22, no. 8, pp. 969–976, Aug. 2004.
- [98] M.-K. So, C. Xu, A. M. Loening, S. S. Gambhir, and J. Rao, “Self-illuminating quantum dot conjugates for *in vivo* imaging,” *Nature Biotechnology*, vol. 24, no. 3, pp. 339–343, Mar. 2006.
- [99] X. Michalet *et al.*, “Quantum dots for live cells, *in vivo* imaging, and diagnostics,” *Science*, vol. 307, no. 5709, pp. 538–544, 2005.

- [100] G. G. See *et al.*, “Region specific enhancement of quantum dot emission using interleaved two-dimensional photonic crystals,” *Applied Optics*, vol. 54, no. 9, pp. 2302–2308, Mar. 2015.
- [101] G. G. See *et al.*, “Enhanced emission of quantum dots embedded within the high-index dielectric regions of photonic crystal slabs,” *Applied Physics Letters*, vol. 108, no. 17, p. 171108, Apr. 2016.
- [102] N. Ganesh *et al.*, “Enhanced fluorescence emission from quantum dots on a photonic crystal surface,” *Nature Nanotechnology*, vol. 2, no. 8, pp. 515–520, Aug. 2007.
- [103] F. Yang and B. T. Cunningham, “Enhanced quantum dot optical down-conversion using asymmetric 2D photonic crystals,” *Optics Express*, vol. 19, no. 5, p. 3908, Feb. 2011.
- [104] D. Englund *et al.*, “Controlling the spontaneous emission rate of single quantum dots in a two-dimensional photonic crystal,” *Physical Review Letters*, vol. 95, no. 1, p. 013904, July 2005.
- [105] P. Lodahl *et al.*, “Controlling the dynamics of spontaneous emission from quantum dots by photonic crystals,” *Nature*, vol. 430, no. 7000, pp. 654–657, Aug. 2004.
- [106] H. Mohammadi and E. Eslami, “Investigation of spectral resolution in a Czerny Turner spectrograph,” *Instruments and Experimental Techniques*, vol. 53, no. 4, pp. 549–552, July 2010.
- [107] Q. Zhang, Y. Li, and R. W. Tsien, “The dynamic control of kiss-and-run and vesicular reuse probed with single nanoparticles,” *Science*, vol. 323, no. 5920, pp. 1448–1453, Mar. 2009.
- [108] M. A. Thompson, M. D. Lew, M. Badieirostami, and W. E. Moerner, “Localizing and tracking single nanoscale emitters in three dimensions with high spatiotemporal resolution using a double-helix point spread function,” *Nano Letters*, vol. 10, no. 1, pp. 211–218, Jan. 2010.
- [109] J. C. Chang and S. J. Rosenthal, “Single quantum dot imaging in living cells,” *Methods in Molecular Biology*, vol. 991, pp. 149–162, 2013.
- [110] Y. He, S. He, and X. Yang, “Optical field enhancement in nanoscale slot waveguides of hyperbolic metamaterials,” *Optics Letters*, vol. 37, no. 14, pp. 2907–9, July 2012.
- [111] T. Galfsky *et al.*, “Broadband enhancement of spontaneous emission in two-dimensional semiconductors using photonic hypercrystals,” *Nano Letters*, vol. 16, no. 8, pp. 4940–4945, Aug. 2016.

- [112] Z. Huang and E. E. Narimanov, “Optical imaging with photonic hypercrystals: Veselago lens and beyond,” *Journal of Optics*, vol. 16, no. 11, p. 114009, Nov. 2014.
- [113] Y. C. Chang, A. V. Kildishev, E. E. Narimanov, and T. B. Norris, “Metasurface perfect absorber based on guided resonance of a photonic hypercrystal,” *Physical Review B - Condensed Matter and Materials Physics*, vol. 94, no. 15, p. 155430, June 2016.
- [114] A. J. Hoffman *et al.*, “Negative refraction in semiconductor metamaterials,” *Nature Materials*, vol. 6, no. 12, pp. 946–50, Dec. 2007.
- [115] V. Liu and S. Fan, “S⁴: A free electromagnetic solver for layered periodic structures,” *Computer Physics Communications*, vol. 183, no. 10, pp. 2233–2244, Oct. 2012.
- [116] A. D. Rakic *et al.*, “Optical properties of metallic films for vertical-cavity optoelectronic devices,” *Applied Optics*, vol. 37, no. 22, p. 5271, Aug. 1998.
- [117] E. J. Zeman and G. C. Schatz, “An accurate electromagnetic theory study of surface enhancement factors for silver, gold, copper, lithium, sodium, aluminum, gallium, indium, zinc, and cadmium,” *The Journal of Physical Chemistry*, vol. 91, no. 3, pp. 634–643, Jan. 1987.
- [118] H. U. Yang *et al.*, “Optical dielectric function of silver,” *Physical Review B*, vol. 91, no. 23, p. 235137, June 2015.
- [119] D. I. Yakubovsky, A. V. Arsenin, Y. V. Stebunov, D. Y. Fedyanin, and V. S. Volkov, “Optical constants and structural properties of thin gold films,” *Optics Express*, vol. 25, no. 21, p. 25574, Oct. 2017.
- [120] P. Kelly, D. White, and L. Kuznetsova, “Theoretical design of nano-layered Al/SiO₂ metamaterial with hyperbolic dispersion with minimum losses,” in *Proc. SPIE 9495, Nanophotonic Materials XII*, Oct. 2015, p. 95450B.
- [121] R.-L. Chern, “Spatial dispersion and nonlocal effective permittivity for periodic layered metamaterials,” *Optics Express*, vol. 21, no. 14, p. 16514, July 2013.
- [122] J. Elser, V. A. Podolskiy, I. Salakhutdinov, and I. Avrutsky, “Nonlocal effects in effective-medium response of nanolayered metamaterials,” *Applied Physics Letters*, vol. 90, no. 19, p. 191109, May 2007.
- [123] T. Galfsky *et al.*, “Active hyperbolic metamaterials: enhanced spontaneous emission and light extraction,” *Optica*, vol. 2, no. 1, p. 62, Jan. 2015.

- [124] A. T. Voutsas, Y. Hibino, R. Pethe, and E. Demaray, "Structure engineering for hillock-free pure aluminum sputter deposition for gate and source line fabrication in active-matrix liquid crystal displays," *Journal of Vacuum Science & Technology A: Vacuum, Surfaces, and Films*, vol. 16, no. 4, p. 2668, July 1998.
- [125] A. Kamijo and T. Mitsuzuka, "A highly oriented Al[111] texture developed on ultrathin metal underlayers," *Journal of Applied Physics*, vol. 77, no. 8, pp. 3799–3804, Apr. 1995.
- [126] R. S. Bauer, R. Z. Bachrach, and L. J. Brillson, "Au and Al interface reactions with SiO₂," *Applied Physics Letters*, vol. 37, no. 11, pp. 1006–1008, Dec. 1980.
- [127] Y. Miura and K. Hirose, "Direct observation of a thin reacted layer buried at Al/SiO₂ interfaces," *Journal of Applied Physics*, vol. 77, no. 7, pp. 3554–3556, Apr. 1995.
- [128] M. H. Hecht, R. P. Vasquez, F. J. Grunthaner, N. Zamani, and J. Maserjian, "A novel x-ray photoelectron spectroscopy study of the Al/SiO₂ interface," *Journal of Applied Physics*, vol. 57, no. 12, pp. 5256–5261, June 1985.
- [129] K. R. Williams, K. Gupta, and M. Wasilik, "Etch rates for micromachining processing - part II," *Journal of Microelectromechanical Systems*, vol. 12, no. 6, pp. 761–778, Dec. 2003.
- [130] C. J. Ryan *et al.*, "Abiraterone in metastatic prostate cancer without previous chemotherapy," *New England Journal of Medicine*, vol. 368, no. 2, pp. 138–148, 2013.
- [131] J. S. de Bono *et al.*, "Abiraterone and increased survival in metastatic prostate cancer," *New England Journal of Medicine*, vol. 364, no. 21, pp. 1995–2005, 2011.
- [132] H. I. Scher *et al.*, "Increased survival with enzalutamide in prostate cancer after chemotherapy," *New England Journal of Medicine*, vol. 367, no. 13, pp. 1187–1197, Sep. 2012.
- [133] T. M. Beer *et al.*, "Enzalutamide in metastatic prostate cancer before chemotherapy," *New England Journal of Medicine*, vol. 371, no. 5, pp. 424–433, July 2014.
- [134] P. W. Kantoff *et al.*, "Sipuleucel-t immunotherapy for castration-resistant prostate cancer," *New England Journal of Medicine*, vol. 363, no. 5, pp. 411–422, July 2010.

- [135] J. S. de Bono *et al.*, “Prednisone plus cabazitaxel or mitoxantrone for metastatic castration-resistant prostate cancer progressing after docetaxel treatment: A randomised open-label trial,” *The Lancet*, vol. 376, no. 9747, pp. 1147–1154, Oct. 2010.
- [136] A. Anantharaman and T. W. Friedlander, “Targeting the androgen receptor in metastatic castrate-resistant prostate cancer: A review,” *Urologic Oncology: Seminars and Original Investigations*, vol. 34, no. 8, pp. 356–367, Aug. 2016.
- [137] H. I. Scher *et al.*, “Design and end points of clinical trials for patients with progressive prostate cancer and castrate levels of testosterone: Recommendations of the prostate cancer clinical trials working group,” *Journal of Clinical Oncology*, vol. 26, no. 7, pp. 1148–1159, 2008.
- [138] G. Galletti, B. I. Leach, L. Lam, and S. T. Tagawa, “Mechanisms of resistance to systemic therapy in metastatic castration-resistant prostate cancer,” *Cancer Treatment Reviews*, vol. 57, pp. 16–27, June 2017.
- [139] A. A. Shafi, A. E. Yen, and N. L. Weigel, “Androgen receptors in hormone-dependent and castration-resistant prostate cancer,” *Pharmacology & Therapeutics*, vol. 140, no. 3, pp. 223–238, Dec. 2013.
- [140] J. Lu, T. Van Der Steen, D. J. Tindall, T. V. der Steen, and D. J. Tindall, “Are androgen receptor variants a substitute for the full-length receptor?” *Nature Reviews Urology*, vol. 12, no. March, pp. 137–144, Feb. 2015.
- [141] R. J. Andersen *et al.*, “Regression of castrate-recurrent prostate cancer by a small-molecule inhibitor of the amino-terminus domain of the androgen receptor,” *Cancer Cell*, vol. 17, no. 6, pp. 535–546, June 2010.
- [142] E. S. Antonarakis *et al.*, “AR-V7 and resistance to enzalutamide and abiraterone in prostate cancer,” *New England Journal of Medicine*, vol. 371, no. 11, pp. 1028–1038, Sep. 2014.
- [143] E. S. Antonarakis *et al.*, “Androgen receptor splice variant 7 and efficacy of taxane chemotherapy in patients with metastatic castration-resistant prostate cancer,” *JAMA Oncology*, vol. 1, no. 5, p. 582, Aug. 2015.
- [144] F. Qu *et al.*, “Association of AR-V7 and prostate-specific antigen RNA levels in blood with efficacy of abiraterone acetate and enzalutamide treatment in men with prostate cancer,” *Clinical Cancer Research*, vol. 23, no. 3, pp. 726–734, Feb. 2017.
- [145] J. Das *et al.*, “An electrochemical clamp assay for direct, rapid analysis of circulating nucleic acids in serum,” *Nature Chemistry*, vol. 7, no. 7, pp. 569–575, June 2015.

- [146] H. Schwarzenbach, D. S. B. Hoon, and K. Pantel, “Cell-free nucleic acids as biomarkers in cancer patients,” *Nature Reviews Cancer*, vol. 11, no. 6, pp. 426–437, June 2011.
- [147] D. C. Tkachuk, D. Pinkel, W. L. Kuo, H. U. Weier, and J. W. Gray, “Clinical applications of fluorescence in situ hybridization,” *Genetic Analysis Techniques and Applications*, vol. 8, no. 2, pp. 67–74, Apr. 1991.
- [148] S. Haile and M. D. Sadar, “Androgen receptor and its splice variants in prostate cancer,” *Cellular and Molecular Life Sciences*, vol. 68, no. 24, pp. 3971–3981, Dec. 2011.
- [149] H. T. Nguyen *et al.*, “Microfluidics-assisted fluorescence in situ hybridization for advantageous human epidermal growth factor receptor 2 assessment in breast cancer,” *Laboratory Investigation*, vol. 97, no. 1, pp. 93–103, Jan. 2017.
- [150] A. M. Femino, F. S. Fay, K. Fogarty, and R. H. Singer, “Visualization of single RNA transcripts in situ,” *Science*, vol. 280, no. 5363, pp. 585–590, 1998.
- [151] A. Ros-García, A. Nicolás, A. L. García-Pérez, R. A. Juste, and A. Hurtado, “Development and evaluation of a real-time PCR assay for the quantitative detection of theileria annulata in cattle,” *Parasites & Vectors*, vol. 5, no. 1, pp. 1–8, Aug. 2012.
- [152] C. M. Hindson *et al.*, “Absolute quantification by droplet digital PCR versus analog real-time PCR,” *Nature Methods*, vol. 10, no. 10, pp. 1003–1005, Sep. 2013.
- [153] V. Marx, “PCR: paths to sensitivity,” *Nature Methods*, vol. 11, no. 3, pp. 241–245, Feb. 2014.
- [154] A. P. Alivisatos, W. Gu, and C. Larabell, “Quantum dots as cellular probes,” *Annual Review of Biomedical Engineering*, vol. 7, no. 1, pp. 55–76, Aug. 2005.
- [155] S. Pathak, S. K. Choi, N. Arnheim, and M. E. Thompson, “Hydroxylated quantum dots as luminescent probes for in situ hybridization,” *Journal of the American Chemical Society*, vol. 123, no. 17, pp. 4103–4104, 2001.
- [156] B. A. Kairdolf *et al.*, “Semiconductor quantum dots for bioimaging and biodiagnostic applications,” *Annual Review of Analytical Chemistry*, vol. 6, no. 1, pp. 143–162, June 2013.
- [157] L. Ma *et al.*, “Multidentate polymer coatings for compact and homogeneous quantum dots with efficient bioconjugation,” *Journal of the American Chemical Society*, vol. 138, no. 10, pp. 3382–3394, Mar. 2016.